




JGR Solid Earth

RESEARCH ARTICLE

10.1029/2020JB021226

Fourteen-Year Acceleration Along the Japan Trench

Lou Marill¹ , David Marsan¹ , Anne Socquet¹ , Mathilde Radiguet¹ ,
Nathalie Cotte¹ , and Baptiste Rousset¹ 

¹University of Grenoble Alpes, University Savoie Mont Blanc, CNRS, IRD, University of Gustave Eiffel, Grenoble, France

Special Section:

Creep on continental faults and subduction zones: Geophysics, geology, and mechanics

Key Points:

- We reveal a novel and robust acceleration of the surface displacement in the Kanto area over 1997–2011
- We infer a slip rate acceleration along the Pacific-North America subduction interface, both offshore Kanto and Tohoku regions
- We propose a simple relationship that relates the observations with changes in seismicity and slip rates

Supporting Information:

Supporting Information may be found in the online version of this article.

Correspondence to:

L. Marill,
lou.marill@univ-smb.fr

Citation:

Marill, L., Marsan, D., Socquet, A., Radiguet, M., Cotte, N., & Rousset, B. (2021). Fourteen-year acceleration along the Japan Trench. *Journal of Geophysical Research: Solid Earth*, 126, e2020JB021226. <https://doi.org/10.1029/2020JB021226>

Received 21 OCT 2020

Accepted 29 SEP 2021

Abstract An acceleration of the background seismicity and a shortening of the slow slip events recurrence intervals in the Boso peninsula (Japan) suggest a slow unlocking of the Philippine Sea-North America (PHS-NAM) subduction interface from 1990 to 2011. Motivated by these previous observations, we used GPS (Global Positioning System) time series to study the 1997–2011 evolution of interface locking offshore Honshu with a specific focus on the Kanto region. We newly processed the GPS data in double difference and analyzed them with a trajectory model that accounts for seismic and aseismic variations, and that includes an inter-seismic acceleration term. We inverted the surface acceleration obtained, on both the Pacific-North America (PAC-NAM) and the PHS-NAM interfaces. The inverted slip rate changes over time compare well with previous studies: we infer slip deceleration between 39°–41°N and acceleration between 37°–38°N (PAC-NAM), with a maximum amplitude of 1.75 mm/yr² corresponding to an equivalent geodetic locking change of 0.3 over the 14 years. More notably, our analysis reveals a novel and robust slip acceleration South of 36°N that we interpret as an unlocking of the PAC-NAM interface. It is located noticeably far from the 2011 Tohoku earthquake rupture and is therefore unlikely connected to it. The slip acceleration inverted from the surface displacements is comparable to the changes observed in the seismicity rate. Our results further demonstrate that inter-seismic slip rate can significantly evolve over years to decades, and suggest a simple relationship between the seismicity and the slip on the subduction interface.

Plain Language Summary Subduction zones, where an oceanic plate dives under a continental plate, host both seismic and aseismic slip events. In Japan, along the Sagami Trough where the Philippine Sea (PHS) plate subducts beneath the North America (NAM) plate, the increase of the number of earthquakes between 1990 and 2011 suggests that the PHS plate slips at a higher rate under the NAM plate. Along the Japan Trench, North of the Sagami Trough, the Pacific (PAC) plate subducts beneath the NAM plate; changes in the slip rate of the PAC plate have already been inferred from geodetic measurements by previous studies. To further investigate those changes in slip rate at both interfaces, we processed and analyzed GPS (Global Positioning System) time series from 1997 to 2011, and compared them with changes in earthquake rates. From those time series, we determine the slip rate of the continental plate. On the PAC-NAM interface, the slip either decelerates or accelerates depending on the location. Most notably, our analysis reveals a novel slip acceleration near the Boso peninsula that we interpret as an acceleration of the PAC plate's slip beneath the NAM plate, proving that plates can subduct at non-stationary velocities.

1. Introduction

A common assumption regarding the seismic cycle is to consider the inter-seismic strain rate as being constant over time (Savage & Thatcher, 1992). Recently, long-term changes in slip rate, or interface locking, have been inferred or suggested in the context of subduction zones. Long-term slow slip events (L-SSEs) with a duration of a few years have been documented in Alaska (duration of 2–9 years) (Li et al., 2016; Rousset et al., 2019) and in various regions of Japan (e.g., Tokai district, Kanto region, Kii peninsula, and Bungo channel, with duration from 1 to 5 years) (Hirose et al., 1999; Kobayashi, 2014; Kobayashi & Tsuyuki, 2019; Miyazaki et al., 2003; Ochi & Kato, 2013; Ozawa et al., 2001, 2013; Ozawa, Suito, Imakiire, & Murakami, 2007; Tanaka & Yabe, 2017; Yagi & Kikuchi, 2003; Yoshioka et al., 2015). Variations at even longer time scales (decades) have also been inferred. In Sumatra, Prawirodirdjo et al. (2010) infer a decrease of locking between the 1990s and 2010 in the Batu and Enggano islands. Based on coral observations that

allow the estimation of relative sea-level changes, Meltzner et al. (2015) document changes in subsidence rate along the Sunda Trench offshore Sumatra, with significant variations in the inter-seismic rate over ~200 years. A 15-year-long (1966–1981) SSE was proposed to explain the observations in the Banyak Islands, located above the rupture zone of the 2005 M_w 8.6 earthquake (see also Tsang et al., 2015), although the 25 years gap between the two events challenges the existence of a causal link. Some of the long-term variations could however be more directly related to subsequent megathrust earthquakes: a 32-year long surface deformation anomaly was interpreted as an SSE in the shallow part of the plate interface, before the 1861 M 8.5 megathrust earthquake (Mallick et al., 2021); the authors propose that this long duration SSE could have been triggered and sustained by elevated pore fluid pressure, and then stopped by subsequent drainage caused by the mainshock. In Japan, Hasegawa and Yoshida (2015), Heki and Mitsui (2013), Loveless and Meade (2016), Mavrommatis et al. (2014), Mavrommatis et al. (2015), and Yokota and Koketsu (2015) infer slip rate variations over 15 years along the Japan Trench before the 2011 Tohoku earthquake. At the Mendocino triple junction, Materna et al. (2019) document slip rate variations between four $M \geq 6.5$ regional earthquakes from 2005 to 2019. In South America, Melnick et al. (2017) and Ruiz et al. (2017) identify a change in loading rate likely triggered by the 2010 M_w 8.8 Maule earthquake. This change is seen up to the 2015 M_w 8.3 Illapel earthquake North of Maule rupture (Melnick et al., 2017) and up to the 2016 M_w 7.6 Chiloé earthquake South (Ruiz et al., 2017).

The mechanisms responsible for such variations in inter-seismic slip rate at the decadal time scale are yet to be understood. Since they overlap the time scale of post-seismic, and, more generally, of crustal and upper-mantle visco-elastic relaxation processes, they could be related to recent earthquakes and mega-thrust earthquakes, as previously suggested by Heki and Mitsui (2013) or Melnick et al. (2017). Variations that precede, rather than follow, large earthquakes are yet to be interpreted in terms of dynamical processes, which could conceivably be similar to those controlling SSEs of much shorter durations. In any case, dynamical modeling and physical understanding of these phenomena first require well constrained kinematic observations.

We here present a study of inter-seismic slip rate changes at the Japan Trench—North America (NAM) plate and Pacific (PAC) plate interface—and the Sagami Through—NAM plate and Philippine Sea (PHS) plate interface—subduction zones (Figure 1), from January 1, 1997 to February 6, 2011. As large scale variations in geodetic movements can be caused by reference frame issues, a first goal of this study is to provide a full re-analysis of the Japanese GPS data that is completely independent of the F3 solution (Nakagawa et al., 2009) on which are based previous studies of decadal slip rate variations (Mavrommatis et al., 2014; Yokota & Koketsu, 2015). The second goal is to complement the observations of Mavrommatis et al. (2014) and Yokota and Koketsu (2015) by extending the investigation of the surface displacements to the Kanto region (Figure 1). This region is known to have undergone a strong acceleration of the background seismicity rate on both PHS and PAC plates (Marsan et al., 2017; Reverso et al., 2016), as well as a shortening of the Boso SSEs recurrence times from 1996 to 2011 on the PHS plate (Fukuda, 2018; Gardonio et al., 2018; Hirose et al., 2012). These observations suggest that plate unlocking, involving the three tectonic plates that control surface deformation in Kanto (the NAM, PAC, and PHS plates), has been going on for at least a decade before the 2011 M_w 9.0 Tohoku earthquake. Given the distance between the Kanto region and potential mainshock candidates that could possibly explain the northern Honshu changes in slip rate (namely, the 2003 M_w 8.0 Tokachi earthquake, see Figure 1), any variation in local slip rate in Kanto could not be conceivably related to unmodeled post-seismic processes of such mainshocks. The Kanto region is therefore a natural candidate to study possible decadal slip rate variations. The third goal of this study is to compare the evolution of the slip on the subduction interface derived from surface displacements to the variations of the seismicity rate, and to propose a simple relationship that relates both observables.

In more detail, this study complements the analyses of Mavrommatis et al. (2014) and Yokota and Koketsu (2015) by (a) performing a re-analysis of the GPS data, (b) including the Kanto region, and (c) testing the sensitivity of the inverted changes in slip rate relative to the inclusion of slip on the PHS plate, of different a priori distributions, including a seismicity-based prior, and of GPS vertical components. After summarizing the tectonic setting of the Honshu island (Section 2), we describe our processing and analysis of GPS data (Section 3) as well as the inversion of slip rate distribution (Section 4). We then analyze the mean surface velocity and the acceleration fields, and infer the inter-seismic locking, the locking difference between 2011

Honshu Tectonic Setting

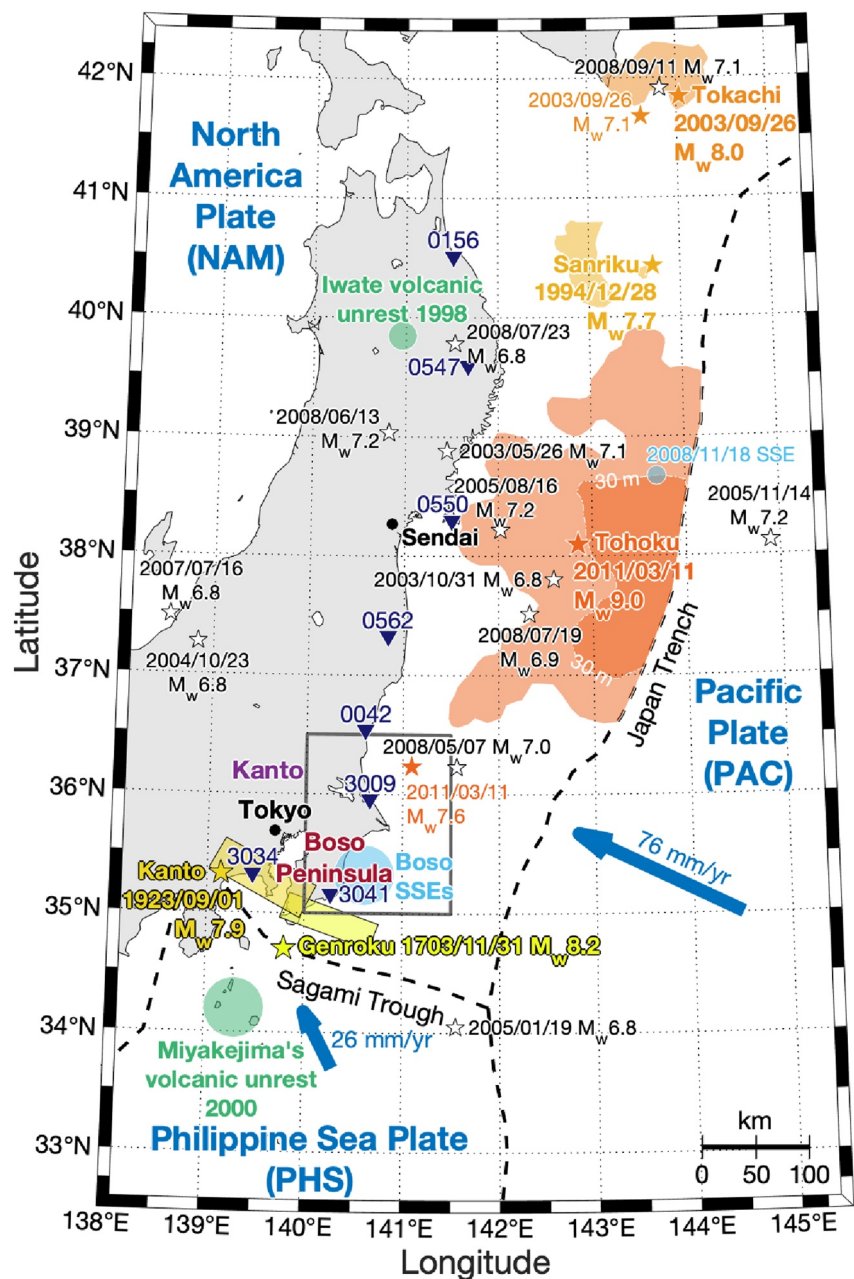


Figure 1. Tectonic setting of Honshu island. The colored stars represent the historical and instrumentally recorded great earthquakes, $M_w \geq 7.7$, as well as major aftershocks; format date is year/month/day; ruptured areas are also indicated (same color as the corresponding star) (Hooper et al., 2013; A. Ito et al., 2004; Komori et al., 2017; Shishikura, 2014; Yamanaka & Kikuchi, 2003). The 1703 Genroku earthquake broke the two yellow patches. The white stars represent the $M_w \geq 6.8$ earthquakes occurring between 1996 and 2011. The blue circle near the Boso peninsula represents the Boso SSEs rupture area (Fukuda, 2018), and the one at 38.67°N and 143.70°E represents the location of another SSE occurring in 2008 (Y. Ito et al., 2013). The green circles represent the location of two volcanic unrests: the 2000 Miyakejima volcanic unrest (Cattania et al., 2017) and the 1998 Iwate volcanic unrest (Miura et al., 2000). The navy triangles correspond to the stations shown in Figures 2 and 3. The continuous gray square is the Figure 8a zoom. Plate motions are deduced from Nishimura et al. (2007)'s Euler poles.

Table 1
Euler Rotation Poles

Plate	Reference plate	Latitude	Longitude	Rotation rate
		deg	deg	deg/Ma
NAM ^a	EUR	75.85	130.92	−0.351
PAC	EUR	63.10	79.20	−0.919
PHS	EUR	36.61	138.96	−9.956

Note. From Nishimura et al. (2007). EUR, Eurasia plate; NAM, North America plate; PAC, Pacific plate; PHS, Philippine Sea plate.

^aNAM corresponds to the Central Japan Block (CJB) in Nishimura et al. (2007).

and 1997, and the slip acceleration on the megathrust interface (Section 5). We discuss the robustness of our obtained slip acceleration (Section 5.3) and its relationship with regional seismicity (Section 6). Finally, we interpret the results in light of both the subsequent rupture of the 2011 M_w 9.0 Tohoku earthquake and the acceleration in the wider Kanto region (Section 7).

2. Honshu Tectonic Setting

The subduction of the PAC plate beneath the NAM plate induced the following great instrumentally recorded earthquakes: the 1994 M_w 7.7 Sanriku earthquake (A. Ito et al., 2004), the 2003 M_w 8.0 Tokachi earthquake (Yamanaka & Kikuchi, 2003), and the 2011 M_w 9.0 Tohoku earthquake (Hooper et al., 2013) (Figure 1). While the 1994 Sanriku and the 2003 Tokachi earthquakes mostly affected the northern part of Honshu and Hok-

kaido, the 2011 Tohoku earthquake ruptured a large part of the Japan Trench and impacted all the North of Honshu, the rupture itself terminating not far from the Kanto region (see Lay, 2018 for a review on the 2011 mainshock). The reader is referred to Suito et al. (2011) for a more detailed account of earthquake activity in this zone before 2011. Two great known historical earthquakes struck the Kanto region, at the interface between the PHS plate and the NAM plate: the 1703 M_w 8.2 Genroku Kanto earthquake (named Genroku in Figure 1) and the 1923 M_w 7.9 Taisho Kanto earthquake (named Kanto in Figure 1) (Komori et al., 2017; Shishikura, 2014). These two earthquakes outline resisting asperities on the PHS plate which are expected to appear as strongly locked in inter-seismic locking models (see Philibosian & Meltzner, 2020 for a more detailed account of past ruptures along the Sagami Trough).

There are many transient deformation events affecting the land-based GPS sites. Recurrent SSEs have been occurring on the PHS plate offshore Boso peninsula with a recurrence interval of ~6 years between 1983 and 2007 (Hirose et al., 2012; Ozawa, Suito, & Tobita, 2007). These SSEs ruptured roughly the same area (blue circle named Boso SSEs in Figure 1), had a characteristic size ($M_w \sim 6.6$) and lasted from 14 days (in 1996 and 2007) to 43 days (in 2002) (Fukuda, 2018). Another SSE occurred in 2008 but at 38.67°N and 143.70°E on the PAC-NAM interface (thereafter named the Tohoku SSE), and impacted the stations North of Honshu (Y. Ito et al., 2013). Finally, two important volcanic unrests happened: one at the Iwate volcano in 1998 (thereafter named the 1998 Iwate volcanic unrest, see Figure 1) (Miura et al., 2000) and the other one around Miyakejima island in 2000 (thereafter named the 2000 Miyakejima volcanic unrest, see Figure 1) (Cattania et al., 2017; Ito & Yoshioka, 2002). Both were associated with an intense seismicity swarm. For example, over 100,000 earthquakes occurred in a 2-month period during the 2000 Miyakejima volcanic unrest, including five $M_w > 6.0$ earthquakes (T. Ito & Yoshioka, 2002) for a total seismic moment release estimated to $M_0 = 3.6 \times 10^{19}$ N m (Cattania et al., 2017). The Miyakejima volcanic unrest was large enough to impact the surface displacement of the NAM plate up to 37°N, and produced a large transient deformation with centimetric displacements recorded on the Boso peninsula.

Plate convergence is computed using Nishimura et al. (2007)'s Euler poles, as given in Table 1. The corresponding averaged convergence vectors and values are shown in Figure 1; we obtain $v_{PAC} = 76$ mm/yr and $v_{PHS} = 26$ mm/yr.

3. Data Processing and Analysis

3.1. Data Processing

We processed the 1,421 stations of the GNSS (Global Navigation Satellite System) Earth Observation Network System in Japan (GEONET) and 44 IGS (International GNSS Service, <https://www.igs.org/>) sites worldwide, from January 1, 1997 to February 6, 2011 using only GPS (Global Positioning System) satellite system and following a double-difference approach, using the GAMIT/GLOBK software suite (Herring et al., 2015, 2018a, 2018b). As in Herring et al. (2016), we assemble our stations into sub-networks for the daily processing. We reduce 24-hr measurement sessions to daily estimates of station position, choosing the ionosphere-free combination and fixing the ambiguities to integer values. We use precise orbit positions

Table 2
Characteristics of the Slow Deformation Events

Event type	Starting date (t_s)	Center position	M_w	Duration (t_d)
	Year/month/day	Latitude; longitude		days
Iwate volcanic unrest	1998/01/30	39.85; 140.96	6.00 ^a	186
Miyakejima volcanic unrest	2000/06/26	34.20; 139.30	7.00 ^b	64
Boso SSE	2002/10/02	35.30; 140.70	6.67	43
Boso SSE	2007/08/12	35.35; 140.40	6.65	14
Tohoku SSE	2008/11/18	38.67; 143.70	6.80	7
Boso SSE	2009/12/13 ^b	35.35; 140.45	6.10	44 ^b

Note. 1998 Iwate volcanic unrest from Miura et al. (2000); 2000 Miyakejima volcanic unrest from Cattania et al. (2017), Nakada et al. (2005) and Uhira et al. (2005); Boso slow slip events (SSEs) from Fukuda (2018) and Gardonio et al. (2018); Tohoku SSE from Y. Ito et al. (2013).

^aComputed from the total moment release: $M_0 = 3.6 \times 10^{19}$ N m (Cattania et al., 2017). ^bEstimation based on the observed time series displacements.

from the IGS, precise Earth Orientation Parameters from the IERS (International Earth Rotation and Reference Systems Service) bulletin B (monthly), phase centers of the antennas from IGS tables, ocean-tidal loading corrections from the FES2004 (Finite Element Solution) model, as well as atmospheric loading corrections (tidal and non-tidal). Using the Vienna Mapping Function (Boehm et al., 2006), we estimate one tropospheric zenith delay parameter every 2 hr, and one couple of horizontal tropospheric gradients per 24 hr session. We combine the daily sub-network solutions in a regional stabilization approach using the GAMIT/GLOBK software (Herring et al., 2018b) to obtain daily loosely constrained solutions. We derive the time series by expressing the solutions in the ITRF2014 (Altamimi et al., 2017) with a 7-parameter transformation using regional IGS sites. Position outliers were automatically identified and removed using the PYACS package (Python Yet Another Combination Software) (Tran, 2009). We consider as outliers individual values differing by 15 mm or more from the median value within a 20-data point sliding window. Thereafter, the time series are those without outliers.

3.2. Time Series Analysis With a Trajectory Model

In order to relate large earthquakes to potential co-seismic jumps and post-seismic transients in the GPS time series, we make use of the ISC (International Seismological Center) earthquake catalog limited to $M_w \geq 6.4$ earthquakes around Japan (from 28.6° to 47.4°N, and from 126.5° to 149.2°E). Since the ISC provides M_w estimates from several agencies and all the M_w values are generally not identical, we decide to consider only the M_w determined by the Japan Meteorological Agency because we consider them more accurate than the other estimates for Japan. The moment magnitude (M_w) threshold allows to keep only earthquakes with a visible influence on the time series, and avoids over-fitting. The GPS time series can also be affected by slow deformation transients, defined as either (a) slow slip events (SSEs)—offshore Boso peninsula (Fukuda, 2018) and at 38.67°N and 143.70°E (Y. Ito et al., 2013)—, or (b) volcanic unrests—the 1998 Iwate volcanic unrest (Miura et al., 2000), and the 2000 Miyakejima volcanic unrest (Cattania et al., 2017; Nakada et al., 2005; Uhira et al., 2005). The parameters considered for the modeling of those slow deformation events are summarized in Table 2.

We select the 287 stations located in Honshu with a longitude greater than 139°E. This way, we focus our analysis on the Honshu island, including the Kanto region. Most of our selected stations are in common with Loveless and Meade (2010), Mavrommatis et al. (2014), and Yokota and Koketsu (2015). To model the surface displacements from GPS time series, we use a modified version of Bevis and Brown (2014)'s trajectory model:

$$\begin{aligned}
 x(t) = & x_R + v(t - t_R) + \frac{1}{2}a(t - t_R)^2 + \sum_{k=1}^2 \left[s_k \sin(2k\pi(t - t_R)) + c_k \cos(2k\pi(t - t_R)) \right] \\
 & + \sum_{a=1}^{n_A} b_a H(t - t_a) + \sum_{j=1}^{n_J} c_j H(t - t_j) + \sum_{s=1}^{n_S} d_s J(t - t_s) \\
 & + \sum_{i=1}^{n_I} m_i H(t - t_i) \times \log \left(1 + \frac{t - t_i}{T_R} \right)
 \end{aligned} \tag{1}$$

where t is the time in decimal year, t_R is the reference time (January 1, 1997), x_R is the reference position, v is the initial velocity (or the inter-seismic velocity if a is fixed to 0), and a is the inter-seismic acceleration; $\sum_{k=1}^2 \left[s_k \sin(2k\pi(t - t_R)) + c_k \cos(2k\pi(t - t_R)) \right]$ corresponds to the annual ($k = 1$) and semi-annual ($k = 2$) seasonal model; $\sum_{a=1}^{n_A} b_a H(t - t_a)$ accounts for the antenna jumps, where n_A is the number of antenna changes at the station, b_a is the amplitude associated to the Heaviside function H , and t_a is the antenna change time; $\sum_{j=1}^{n_J} c_j H(t - t_j)$ corresponds to the co-seismic jumps model, where n_J is the number of earthquakes influencing the station, c_j , the amplitude associated to H , and t_j , the earthquake time; $\sum_{s=1}^{n_S} d_s J(t - t_s)$ corresponds to the slow deformations model, where n_S is the number of slow deformation events influencing the station, d_s , the amplitude associated to the function J (explicitated hereafter), and t_s , the slow deformation starting time (see Table 2); and $\sum_{i=1}^{n_I} m_i H(t - t_i) \times \log \left(1 + \frac{t - t_i}{T_R} \right)$ corresponds to the post-seismic transients model, where n_I is the number of earthquakes with post-seismic transients influencing the station (i.e., $n_I \leq n_J$), m_i , the amplitude of the transient, T_R , a characteristic time (fixed at 100 days, as this corresponds to the value that best fits the post-seismic signal in the time series), and t_i , the earthquake time.

For the slow deformation events listed in Table 2, we define the function J as:

$$J(t - t_s) = \begin{cases} 0 & \forall t < t_s \\ -\frac{1}{2} \cos(\pi t_{norm}) + \frac{1}{2} & \forall t \in [t_s; t_s + t_d] \\ 1 & \forall t > t_s + t_d \end{cases} \tag{2}$$

where t_d is the duration of the slow deformation events (see Table 2) and $t_{norm} = (t - t_s)/t_d$.

To define the influence radius of an earthquake, we adapted the Nevada Geodetic Laboratory formula (<http://geodesy.unr.edu/explanationofplots.php>) into:

$$r(M_w) = 10^{(0.43M_w - 0.7)/d} \tag{3}$$

where M_w is the moment magnitude of the event, $d = 1.15$ is an empirical parameter, and r is the influence radius (in km) of the event. If the distance between the station and the earthquake epicenter is smaller than r , then we consider that the earthquake influences the station displacement. For the slow deformation events, we use the moment magnitudes as given in Table 2; we moreover added supplementary stations (outside this range) for which we visually observed a transient change in the time series coincident with the slow deformation events.

For the purpose of modeling the time series, we assume that only $M_w \geq 6.8$ earthquakes (white stars in Figure 1, as well as the 2003 Tokachi earthquake and its M_w 7.1 aftershock) can produce significant post-seismic transient deformations. For each of those earthquakes, we keep all stations with the influence radius r as defined above, and model for those stations a post-seismic phase. For the model, we tested different T_R values and also the use of an exponential instead of a logarithmic function, and kept the model minimizing the Root-Mean-Square Error. We therefore fix a unique characteristic time, $T_R = 100$ days, allowing a good fit of the observed post-seismic transients.

The trajectory model parameters (x_R , v , a , s_k , c_k , b_a , c_j , d_s , and m_i) are optimized independently for each station and component using a least-square inversion and following a three step strategy. In the first step, we compute b_a , c_j and d_s optimizing the jumps (from antenna changes and earthquakes) and slow deformation

events locally, that is, using the time series from 200 data points before the event to 200 data points after the end of the event (t_a , t_j or t_s) and computing:

$$x_{\text{jump_window}}(t) = x_R + v(t - t_R) + \sum_{a=1}^{n_a} b_a H(t - t_a) + \sum_{j=1}^{n_j} c_j H(t - t_j) + \sum_{s=1}^{n_s} d_s I(t - t_s) + \sum_{i=1}^{n_i} m_i H(t - t_i) \times \log\left(1 + \frac{t - t_i}{T_R}\right) \quad (4)$$

We first proceed to a local estimate for the jumps affecting the time series. The 400-data point window allows to have a good estimate of the jumps without polluting the estimation with long-term effects. To do so, we go through the time series and take the first jump (antenna change or co-seismic) or slow deformation (hereafter considered as a “jump” also); if there is no jump in the whole time series, the program proceeds to the next step. We consider first a 400-data point window centered on the jump date (t_s). If another jump happens between the first jump and the end of the window, we extend the window with an extra 200 data points after the second jump. We keep extending the window this way until no more jump stays in the last 200 data points of the window. Whenever fewer than the required number of data points are available (at the beginning or end of the analyzed period), we take as many data points as possible. To illustrate this process, Figure 2c shows a window with three jumps (the 2000 Miyakejima volcanic unrest and two antenna changes). Once the window length is fixed, we fit Equation 4 within that window. As given in Equation 4, an inter-seismic velocity v and post-seismic transients are also modeled for the window, to get the most accurate estimate of the jumps as possible. In case there is a post-seismic transient in the window, we force the transient to have the same sign as the associated co-seismic jump ($m_i \times c_j > 0$ for i and j corresponding to the same earthquake), individually for each component (NS, EW, or vertical). Moreover, in this window, we take $T_R = 10$ days because after testing different values we observe a better co-seismic jump estimation with a smaller T_R . The value of the co-seismic estimation is important because the estimation of the post-seismic displacement (in the next step) can vary according to the estimation of the co-seismic jump. Then, we go to the next jump not included in the current window and start again, until it reaches the last jump. Figure 2 illustrates how the fitting and modeling perform for some selected time windows and stations. Once we have the b_a , c_j and d_s optimized for all the jumps of the time series, we remove these jumps to obtain $x_{\text{step1}}(t)$, which is thus the time series corrected for co-seismic offsets, antenna jumps and slow transients (Table 2).

In the second step, we compute m_i by optimizing the values of the post-seismic transients using the time series from 2 years of data before the earthquake to 2 years of data after and fitting:

$$x_{\text{post-seismic_window}} = x_R + v(t - t_R) + \sum_{k=1}^2 \left[s_k \sin(2k\pi(t - t_R)) + c_k \cos(2k\pi(t - t_R)) \right] + m_i H(t - t_i) \times \log\left(1 + \frac{t - t_i}{T_R}\right) \quad (5)$$

We take 2-year data before the earthquake to estimate the seasonal and semi-seasonal terms within the window (or less than 2 years of data depending on data availability), which results in a better estimation of the post-seismic transient. We also take 2 years of data (or less if not available) after the earthquake. If there is another post-seismic transient within the 2 years of data, as for the 400-data jump window, we extend the window to 2-year data after the transient, until there is no post-seismic transient during the last 2 years of data. Then, we iterate this step to all subsequent $M_w \geq 6.8$ earthquakes influencing the station and subtract the modeled post-seismic transients from $x_{\text{step1}}(t)$ to obtain $x_{\text{step2}}(t)$.

In the third step, we model $x_{\text{step2}}(t)$ as:

$$x_{\text{step2}}(t) = x_R + v(t - t_R) + \frac{a}{2}(t - t_R)^2 + \sum_{k=1}^2 \left[s_k \sin(2k\pi(t - t_R)) + c_k \cos(2k\pi(t - t_R)) \right] \quad (6)$$

and compute x_R , v , a , s_k , and c_k by optimizing the seasonal and inter-seismic phenomena using the whole time series. Then we remove these contributions to get the final residuals of our raw time series.

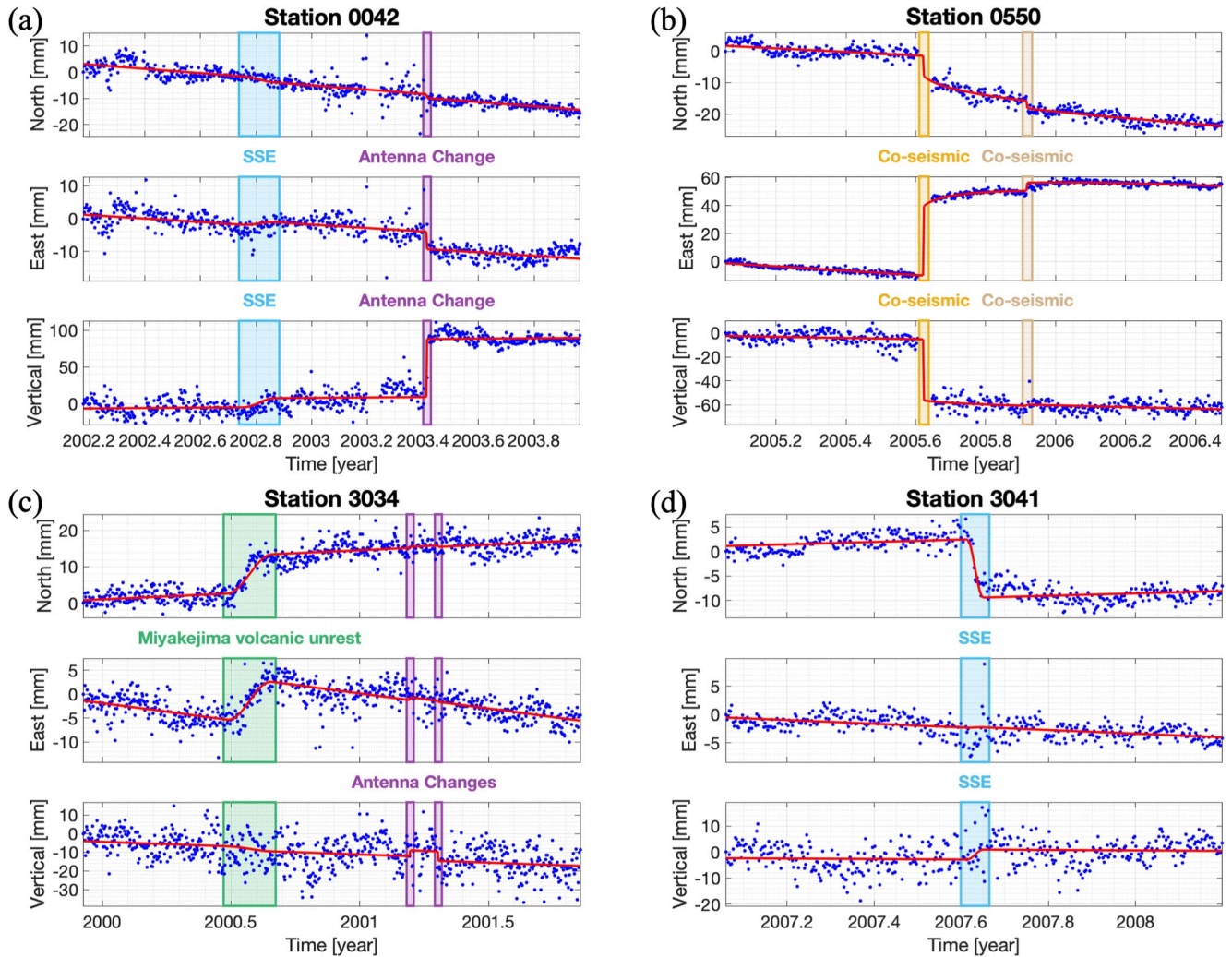


Figure 2. Examples of jumps (antenna changes, earthquakes) and slow deformation (SSEs, volcanic unrest) for the stations 0042 (a), 0550 (b), 3034 (c), and 3041 (d). (a): Model for the 2002 Boso slow slip event (cyan rectangle) and an antenna change (purple rectangle). (b): Model for the 2005 M_w 7.2 Miyagi earthquake (orange rectangle) with post-seismic transient and another M_w 6.6 earthquake (brown rectangle). (c): Model for the 2000 Miyakejima volcanic unrest (green rectangle) and two antenna changes (purple rectangles). (d): Model for the 2007 Boso slow slip event (cyan rectangle). In (a)–(d), the blue dots represent the position time series and the red line represents the trajectory model of Equation 4.

In Equation 1, we added an acceleration term (a) that is usually absent from trajectory models (Bevis & Brown, 2014). This term is motivated by the observation that the residuals of linear trajectory models ($a = 0$) very often display a decadal curvature (visible in the residuals in Figure 3b) and by previous finding of Heki and Mitsui (2013), Mavrommatis et al. (2014), and Yokota and Koketsu (2015) who have first identified such surface motion acceleration. We add a quadratic term, representative of the acceleration, to test if the inter-seismic velocity could have undergone significant changes in Honshu over the 1997–2011 period. The results of the quadratic model are shown in Figures 3c and 3d. To properly estimate the acceleration, a , we require the time series to have at least 8 years and a half (70%) of data between 1997 and 2011.

3.3. Statistical Significance of the Acceleration

We test the significance of adding a quadratic term using synthetic data. To generate synthetic time series, we first compute the Fourier Transform of the quadratic model residuals and randomize the phase. Finally, the inverse Fourier Transform yields a synthetic time series in which colored noise follows the spectral characteristics of the original residual time series. For each station individually, we generate 100 synthetic

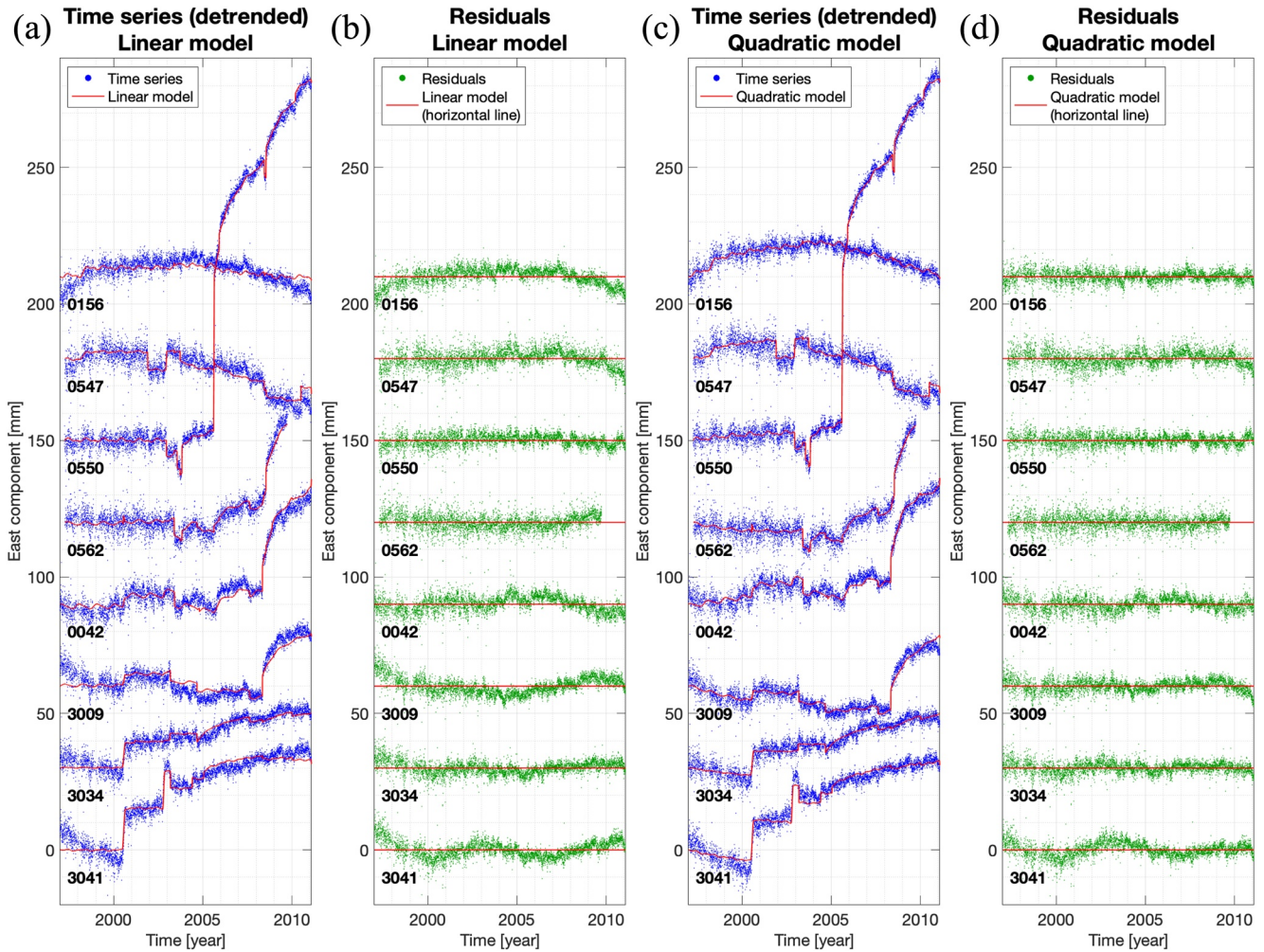


Figure 3. Linear and quadratic trajectory models for the stations shown in Figure 1 (navy triangle), from 1997 to 2011, for the East component. Blue dots represent the raw time series. Red line represents the quadratic trajectory model (Equation 1). Green dots represent the residual time series.

time series, compute the corresponding 100 acceleration terms within this synthetic noise, and determine the standard deviations σ_{a_N} and σ_{a_E} of the 100 North component and 100 East component accelerations, respectively. These standard deviations represent the uncertainties on the acceleration term that can be expected from the noise in our data. They are then compared with the actual accelerations, a_N and a_E (from Equation 1), by computing the signal-to-noise ratios a/σ_a for both components. The stations for which, at least one of the two ratios, $a/\sigma_a > 3$ are considered as showing a significant acceleration. Finally, 221 sites present a significant acceleration, corresponding to 64% of the initial set.

4. Inversion Model of the Loading Rate and Its Acceleration on the Subduction Interface

To determine the average locking and the slip acceleration on the subduction interface, we perform separate least-square slip inversions (Tarantola & Valette, 1982) of the surface velocity and the acceleration fields, respectively, using a modified version of Kositsky and Avouac (2010)'s software package, including the regularization of Radiguet et al. (2011). We only use horizontal displacement time series at this stage; the addition of the vertical displacements will be discussed later (Section 5.2). The forward model is $d = Gm$, where d is the observed data (surface velocity or acceleration field), G , the transfer function matrix computed using Okada (1985), and m , the model on the fault (slip rate or its acceleration, depending on the analysis). The best model (m) is determined using the misfit function:

$$S(m) = \frac{1}{2} \left[(Gm - d)^t C_d^{-1} (Gm - d) + (m - m_0)^t C_m^{-1} (m - m_0) \right] \quad (7)$$

where m_0 is the prior model, C_m is the covariance matrix for the model parameters (detailed in Section 4.4), C_d is the covariance matrix for the data (velocity or acceleration field, detailed in Section 4.3), and t denotes the transpose operation. Minimizing $S(m)$ of Equation 7, we obtain the model function:

$$m = m_0 + C_m G^t (G C_m G^t + C_d)^{-1} (d - G m_0) \quad (8)$$

4.1. Plate Geometry and Imposed Rake

As the Kanto region (Figure 1) is characterized by a double subduction, we run two tests for each inversion (velocity and acceleration fields): (a) considering only the Pacific-North America (PAC-NAM) subduction, and (b) considering both the Philippine Sea-North America (PHS-NAM) and the PAC-NAM subductions. We discretize the faults into triangular sub-fault patches of ~15 km size. For the PAC plate interface, we use the Kamchatka-Kuril Island-Japan region of the Slab 2 model (Hayes et al., 2018). We keep only the part from the Sagami Trough (~34.2°N, see Figure 1) to the North of Honshu island (~41°N), and from the trench down to 90 km depth. For the PHS plate interface, we use Ishida (1992)'s model. For both interfaces, we impose a fixed rake angle for each sub-fault.

To determine this angle, we compute the PAC and PHS plate velocity vectors relative to the NAM plate at each sub-fault using the Euler poles from Nishimura et al. (2007), given in Table 1. Then, we determine the rake, which will be different for each sub-fault, by projecting the velocity vector direction on the sub-fault surface.

4.2. Prior Models

Several prior models have been tested. As default models, we consider (a) a fully locked model for the coupling, hence slip rates equal zero, and (b) a zero acceleration model for the slip acceleration. If the prior is not specified, this default model was applied.

We additionally test a fully unlocked prior model, hence slip rates equal to the convergence rate: this prior brings only small differences in the well-restored area of the PAC plate (Figure S1 in Supporting Information S1). We decided to use the fully locked model as our default model rather than the fully unlocked one because the locking in the not well-restored area is much more likely to be locked. We notice when comparing Figure 4; Figures S2 and S3 in Supporting Information S1, that while changing the PHS plate prior model does not affect the inverted PAC interface locking, the PAC plate prior model impacts the inverted PHS interface locking. Because of this sensitivity to the PAC prior, we must keep in mind that the results for the PHS plate are to be taken with caution.

For the slip acceleration, we test a prior model based on seismicity acceleration to test whether slip and background seismicity are linked. The computation of the seismicity acceleration and the slip acceleration prior model, as well as the inversion results are detailed later in Section 6.

4.3. Data Covariance Matrix

The data covariance matrix (C_d) is a diagonal matrix whose dimension is two times the number of stations, since there are two horizontal channels per station. The diagonal values are determined by the data uncertainties for the North and East components:

$$\forall 0 \leq i \leq n_{sta} - 1, \begin{cases} C_d(2i + 1, 2i + 1) = (errE_i)^2 \\ C_d(2i + 2, 2i + 2) = (errN_i)^2 \end{cases} \quad (9)$$

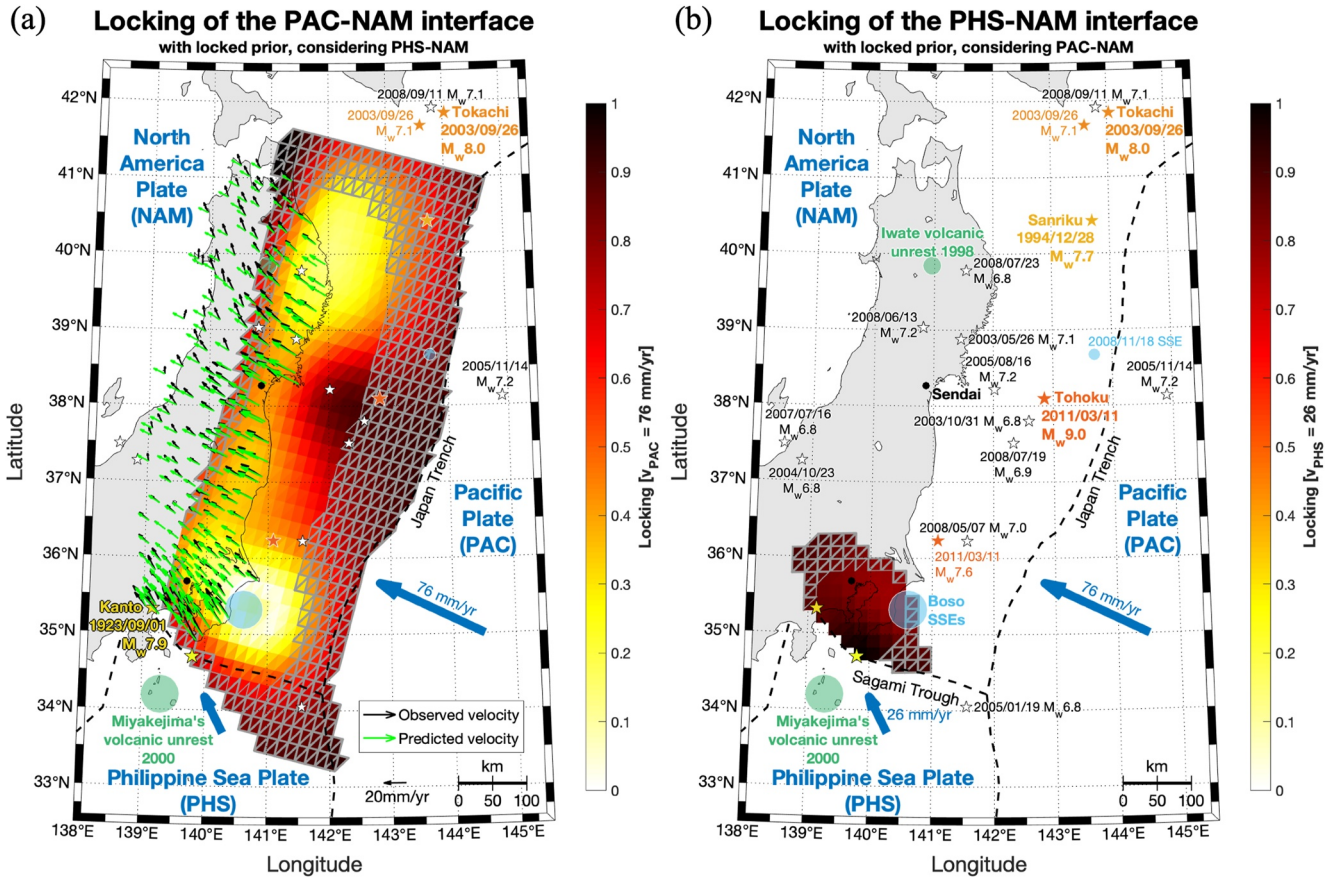


Figure 4. Inter-seismic locking of the Pacific-North America (PAC-NAM) interface (a) and the Philippine Sea-North America (PHS-NAM) interface (b), based on a fully locked prior model. Black arrows: observed velocity field, in a stable NAM reference frame. Green arrows: predicted velocity field. Gray grid: sub-faults for which the slip is poorly restored (see Section 4.5). The amount of locking is shown with the color scale (from freely slipping in white to fully locked in black). The convergence slip rates used to determine the locking of each plate are $v_{PAC} = 76$ mm/yr for the PAC and $v_{PHS} = 26$ mm/yr for the PHS. Other elements are described in Figure 1.

where i is the index of the station, n_{sta} is the number of stations, $errN_i$, the uncertainty of the data i according to the North component, and $errE_i$, the uncertainty of the data i according to the East component.

As velocity uncertainties, we take the RMS of the quadratic model and divide it by the number of data to take into account the data gap. The 5% and 95% quantiles of the horizontal velocity uncertainties are found at 0.14 and 0.27 mm/yr, respectively, with a mean of 0.19 mm/yr. As acceleration uncertainties, we take the standard deviation of the acceleration computed from the synthetic time series (see Section 3.3). The 5% and 95% quantiles of the horizontal acceleration uncertainties are found at 0.010 and 0.126 mm/yr², respectively, with a mean of 0.050 mm/yr².

4.4. Model Covariance Matrix

The model covariance matrix (C_m) introduces two meta-parameters: the standard deviation of the model parameters (σ_m) and the correlation length (λ). We define $C_m(i, j)$, the elements of the model covariance matrix between the sub-faults i and j , based on Radiguet et al. (2011):

$$C_m(i, j) = \sigma_m^2 \times \left(\frac{1}{1 + \frac{\lambda}{\lambda_0}} \right)^2 \exp\left(-\frac{d(i, j)}{\lambda} \right) \quad (10)$$

where λ_0 is a scaling factor fixed to the characteristic sub-fault size (15 km), and $d(i, j)$ is the distance between the centers of sub-faults i and j . The correlation length λ prescribes the distance over which the slip is correlated, and therefore controls the smoothing of the model. For the PAC plate, we use $\lambda = 50$ km corresponding to three times the sub-fault size. For the PHS, we use $\lambda = 240$ km to avoid over-fitting and trade-off issues seen in Section 4.2.

The standard deviation σ_m controls the trade-off between the quality of the fit and the departure from the prior model (m_0). We choose σ_m using a L-curve, namely: L_∞ norm versus χ^2 . The L_∞ norm of the cumulative slip reflects the model roughness, and is defined as:

$$L_\infty = \max_n (|m_n - m_0|) \quad (11)$$

while χ^2 measures the quality of the fit, and is defined as:

$$\chi^2 = \frac{1}{2n_{sta}} \times (Gm - d)^t C_d^{-1} (Gm - d) \quad (12)$$

For the velocity field inversion, we take $\sigma_m = 10^{0.53}$ to limit the slip rate maximum to the plate velocity. Using a fully unlocked prior model for the inversion, the L-curve in Figure S4 in Supporting Information S1 shows that the lowest χ^2 for $L_\infty \leq 76$ mm/yr is obtained for $\sigma_m = 10^{0.53}$. We set the σ_m value for the acceleration inversion based on an argument that relates this value with the $\sigma_m = 10^{0.53}$ value used for the slip rate inversion. We will show later (Figure 5, Section 5.2.2) that the maximum absolute change in seismic locking L between 1997 and 2011 amounts to about $\Delta L = 0.3$. Given the convergence rate $v_{PAC} = 76$ mm/yr for PAC according to NAM, this is equivalent to an acceleration $a_{slip} = 1.75$ mm/yr² at maximum, over $\Delta t = 14.1$ years:

$$a_{slip} = \Delta L \frac{v_{PAC}}{\Delta t} \quad (13)$$

We therefore smooth the inverted slip acceleration so that it can reach 1.75 mm/yr² at maximum, hence $L_\infty \leq 1.75$ mm/yr². Given this constraint, the L-curve (Figure S5 in Supporting Information S1, obtained using a zero-acceleration prior model) gives $\sigma_m = 10^{-0.23}$ for the acceleration inversion. We finally notice that the χ^2 values are large ($\chi^2 = 307$ and $\chi^2 = 16.3$ for the slip rate and the acceleration, respectively), which is due to the relatively small uncertainties we obtain. The latter are likely under-estimated since they only account for estimation, not model, errors. We however use them anyway as they allow to weight (in a relative sense) the inversion; absolute values of χ are therefore of little use here.

4.5. Slip Restitution

For each inversion, we evaluate the resolution by assessing the ability of each sub-fault to resolve a unit slip. We compute the surface displacements caused by a unit slip located on one sub-fault, and invert these displacements using the parameterization previously explained, to obtain a field of slip values. The associated resolution matrix from Tarantola and Valette (1982) is:

$$R = C_m G^t (G C_m G^t + C_d)^{-1} G \quad (14)$$

The resolution matrix diagonal values range from 0 if the slip is not resolved, to one if it is fully resolved. Rather than the resolution itself, we look at the restitution index of the sub-faults corresponding to the sum of R along each row, ranging from 0 to 1.5 (Figure S6 in Supporting Information S1 for the slip rate and Figure S7 in Supporting Information S1 for the slip acceleration). We display with gridded meshes the sub-faults with less than 90% of the slip restored.

5. Analysis and Inversion Results

5.1. Inter-Seismic Velocity Field and Locking

The spatial pattern of the horizontal inter-seismic surface displacements is given by the velocity terms v of the linear trajectory model (Equation 1 when imposing $a = 0$; see Section 3.2; this corresponds to choosing

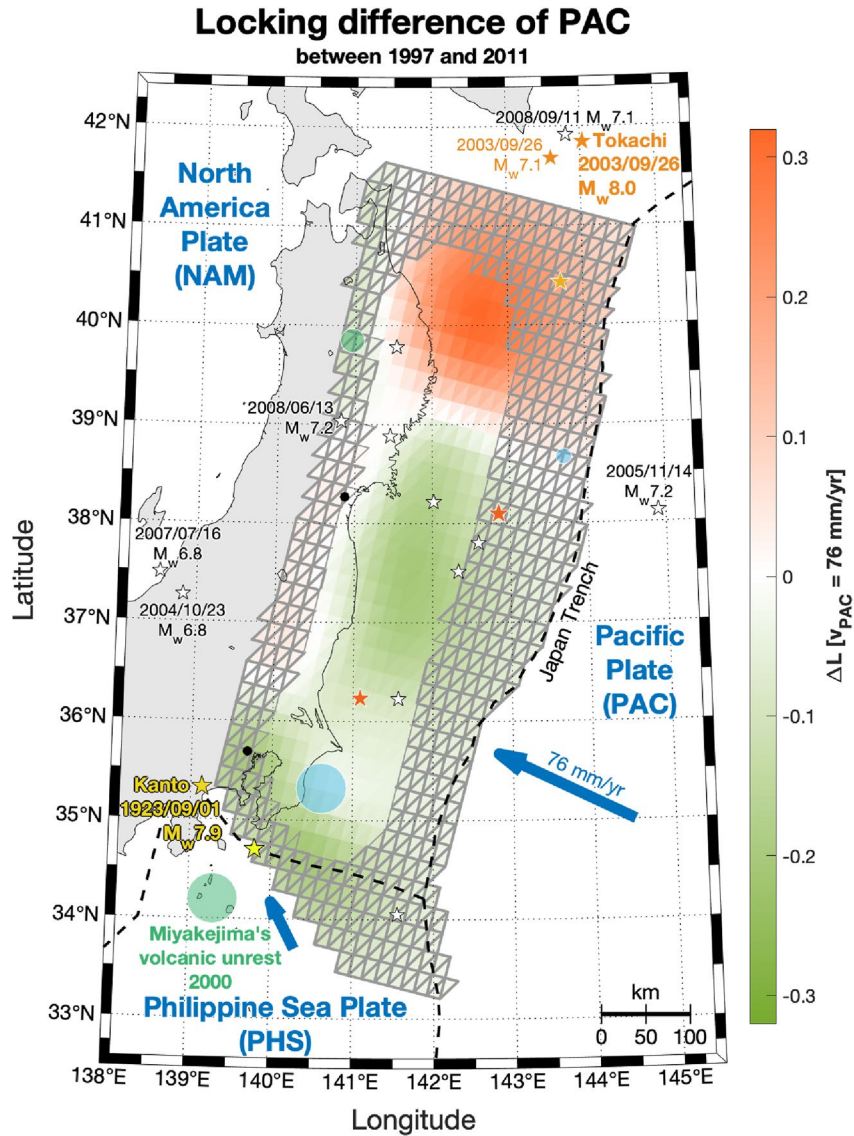


Figure 5. Locking difference ΔL of the Pacific (PAC) plate between 1997 (Figure S8a in Supporting Information S1) and 2011 (Figure S8b in Supporting Information S1). The amount of ΔL on the PAC is shown with the green-orange color scale: orange sub-faults are more locked in 2011 (and green in 1997). The gray grid shows the sub-faults where the slip is poorly restored (see Section 4.5). Other elements are described in Figure 1.

an averaged displacement rate over the 1997–2011 interval. A similar analysis is shown in Figure S8 in Supporting Information S1 when considering either the 1997 or the 2011 displacement rates). To compare our velocity field (Figure 4, black arrows) to the one of Mavrommatis et al. (2014), we transpose our velocity field from ITRF2014 to the NAM reference frame. We compute the velocity of the NAM plate at each station site using the absolute plate rotation poles of the NAM plate in the ITRF2014 given by Altamimi et al. (2017), and we subtract it from our velocity field. The subtraction gives us the velocity field in the NAM reference frame. Figure 4 shows the locking obtained when performing the inversion described in Section 4, with a fully locked prior model, jointly on both the PAC-NAM and the PHS-NAM interfaces. We also show in Figures S9 and S10 in Supporting Information S1 the locking obtained on PAC and PHS for smaller and larger σ_m values, hence allowing for a smoother or rougher locking. Moreover, the locking obtained with a fully unlocked prior model is shown in Figure S1a in Supporting Information S1.

As we present 12 figures (within the main figures and supplementary figures in Supporting Information S1) based on PAC-NAM and/or PHS-NAM locking, we summarize all the model parameters associated with each figure in Table S2 in Supporting Information S1.

5.2. Acceleration Field, Locking Change, and Slip Acceleration

5.2.1. Acceleration Field

Our acceleration field (Figure 6, black and gray arrows) exhibits a landward acceleration North of Honshu with the amplitude decreasing when going West, and a trenchward acceleration South of 38.5°N. The first order of our acceleration pattern and amplitude are compatible with the ones observed by Mavrommatis et al. (2014) and Yokota and Koketsu (2015). Nevertheless, a notable difference is found in the Kanto region, where Yokota and Koketsu (2015) show a very limited acceleration compared to the rest of Honshu. Instead, we find an eastward acceleration with an amplitude of the same order as the north Honshu acceleration. According to our statistical test of the acceleration significance (see Section 3.3) most acceleration values in the Kanto region are significant (Figure 6, black arrows). This acceleration suggests that some plate unlocking took place between 1997 and 2011. We conducted some refined analysis and sensitivity tests, as presented in Section 5.3, to track the origin of this difference but all our tests still show an acceleration in the Kanto region. Ultimately, we cannot reproduce exactly the same analysis as in Mavrommatis et al. (2014) and Yokota and Koketsu (2015) and therefore we cannot determine specifically which difference in our analysis could explain the difference in results.

The vertical accelerations (Figure S11b in Supporting Information S1, outer circles) do not exhibit a spatially coherent pattern, likely because of the noise (that includes all non-tectonic phenomena) contaminating the acceleration signal.

5.2.2. Locking Change

The acceleration observed in the surface deformation implies a change in locking that can be simply evaluated. To do so, we estimate the locking both in 1997 and 2011 using the displacement rates modeled at all stations at the dates January 1, 1997 and February 6, 2011. Namely, we extract the modeled velocity at the first date, which is by definition the linear term of the quadratic model (v in Equation 1), and compute the associated locking (Figure S8a in Supporting Information S1). Adding the acceleration term, we then compute the velocity at the second date as predicted by the trajectory model and invert for the associated locking (Figure S8b in Supporting Information S1). We finally compute the difference in locking ΔL (Figure 5) and find that the maximum in absolute value is $\Delta L = 0.3$ as mentioned in Section 4.4.

5.2.3. Slip Acceleration

We perform a direct estimate of the accelerated slip on the subduction interface. First, we invert the slip acceleration field on the PAC-NAM subduction interface only. Figure 6 shows both accelerated (red) and decelerated (blue) slip rates. The slip acceleration corresponds to an increased forward slip on the subduction interface, or equivalently a decrease in locking. As explained in Section 4.4, a change in locking $\Delta L = 0.3$ over 14 years corresponds to a slip acceleration $a_{slip} = 1.75 \text{ mm/yr}^2$. Then, Figures 5 and 6 display similar relative variations, up to a simple proportionality factor imposed by the convergence rate and the duration of observation (Equation 13).

The residuals between the observed and modeled surface acceleration (Figure S12 in Supporting Information S1) show little spatial coherence at the large scale, implying that the model does well in capturing the large scale pattern, even though the residuals are almost always significantly larger than the uncertainties as discussed in Section 4.4.

A remarkable result is the acceleration area South of 36.5°N, consistent with the observed surface acceleration mentioned earlier. This acceleration remains clearly visible even while varying the σ_m parameter (Figure S13 in Supporting Information S1). Because the presence of the PHS plate cannot be ignored for the stations in Kanto, we perform a second inversion using both the PAC and PHS plates (Figure S14 in Supporting Information S1). Very limited changes are observed, with an increase of the slip acceleration on the PAC plate limited to 0.6 mm/yr^2 at maximum, and a deceleration of the order of 0.3 mm/yr^2 on the

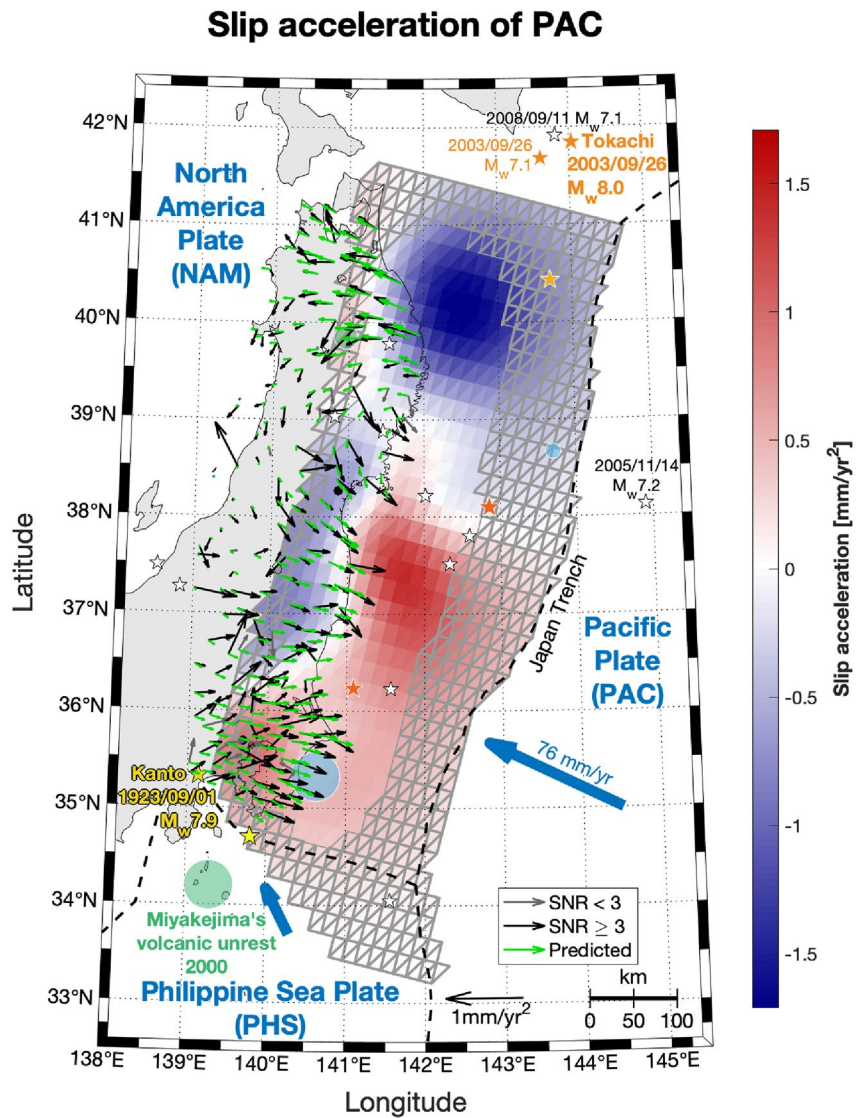


Figure 6. Slip acceleration of the Pacific (PAC) plate with a zero acceleration prior model. The black and gray arrows depict the observed acceleration field: we distinguish the stations which have a signal-to-noise ratio greater than 3 (black), and those which fail to meet this criterion (gray, see Section 3.3). The green arrows represent the acceleration field predicted by the model. The amount of slip acceleration on the PAC slip interface is shown with the blue to red color scale. The gray grid shows the sub-faults for which the slip is poorly restored (see Section 4.5). Other elements are described in Figure 1.

PHS plate. Since a trade-off exists between slip acceleration/deceleration on either plate (see Section 4.2), we cannot resolve with accuracy the proportion of change in slip rate hosted by each plate. Our analysis however clearly demonstrates that there exists a significant increase in slip rate between 1997 and 2011 South of 36.5°N, that is compatible with the observed acceleration of seismicity on the PAC-NAM interface as shown in Marsan et al. (2017).

We also evaluate the impact of adding the vertical displacement to the horizontal ones when inverting for the slip acceleration. Comparing Figure 6 and Figure S11 in Supporting Information S1, we observed that the vertical acceleration has very little effect on the inverted slip acceleration.

As we present nine figures (within the main figures and supplementary figures in Supporting Information S1) based on PAC-NAM and/or PHS-NAM slip acceleration, we summarize all the model parameters associated with each figure in Table S3 in Supporting Information S1.

5.3. Refined Analyses and Sensitivity Tests

We here provide further analyses to compare our results with those of Mavrommatis et al. (2014), Tanaka and Yabe (2017), and Yokota and Koketsu (2015). We notably explore the effects on our results of the reprocessing of the GPS data (Section 5.3.1) and of the inclusion of slow deformation transients in the trajectory model (Section 5.3.2).

5.3.1. This Study's GAMIT/GLOBK Solution Versus F3 Solution

A significant difference with the data presented in Mavrommatis et al. (2014), Tanaka and Yabe (2017), and Yokota and Koketsu (2015) is the GPS solution used. Here, we have done a complete reprocessing of the GPS data, while previous studies used the GEONET F3 solution published by the Geospatial Information Authority of Japan (Nakagawa et al., 2009; Tsuji et al., 2017). Both solutions have been obtained with different processing strategies. Main differences include the use of different softwares (GAMIT/GLOBK vs. Bernese), and the projection in a different version of the International Terrestrial Reference Frame (ITRF2014 vs. ITRF2005) (Altamimi et al., 2007, 2017).

To compare our solution with the F3 solution, we use the Helmert parameters given by the ITRF website (<http://itrf.ensg.ign.fr>) to rotate the F3 solution into the ITRF2014 (more details in Text S1 and Table S1 in Supporting Information S1). Then, we apply the analysis described in Section 3 to the converted F3 solution, by again fitting the trajectory model of Equation 1, and then inverting the acceleration field on the PAC plate (Section 4). The obtained acceleration field, shown in Figure S15 in Supporting Information S1, displays similar first-order features than in Figure 6 and in Mavrommatis et al. (2014) and in Yokota and Koketsu (2015): North of Honshu, the acceleration field is pointing toward the East. The F3 solution implies higher southward acceleration amplitudes (~ 0.5 mm/yr) than our solution as shown by Figure S15a in Supporting Information S1.

The reason for this difference is not clear. It is likely not related to the difference in reference frame, since we have estimated that the transformation from ITRF2005 to ITRF2014 generates average changes in acceleration rate of the order of ~ 0.0001 mm/yr² in Japan. Instead, the F3 solution is clearly more noisy than our solution, notably before 2000, which may lead to different results (see Figure S16 in Supporting Information S1). Indeed, the scatter in 1997 in the F3 solution is almost three times the scatter in 1997 in the GAMIT solution, and even in 2010, the scatter in the F3 solution is two times the one in the GAMIT solution.

5.3.2. Comparison With Previous Studies: Influence of Post-Seismic Modeling and Slow Slip Events

The other differences we find with respect to previous studies (Mavrommatis et al., 2014, 2015; Yokota & Koketsu, 2015) seem to be related to choices made during the time series analysis.

At the latitudes 36.5°–38°N, we find a weaker eastward acceleration than previous studies, both for the GAMIT and F3 data sets (Figure 6; Figures S15a and S16 in Supporting Information S1). This is probably explained by the consideration of different approaches for the post-seismic modeling in the time series analysis. Mavrommatis et al. (2014) perform a physical model for their post-seismic relaxation, while we compute a best fit that is independent from one station to the other. This will naturally lead to the fit of any signal visible in the position time series, and to the reduction of the westward acceleration found in the area, hence of the inverted accelerated slip.

Looking more specifically at Kanto, we observe a significant acceleration with both the F3 and GAMIT solutions (black arrow, Figure 6 and Figure S15 in Supporting Information S1) that were not reported by Mavrommatis et al. (2014) nor by Yokota and Koketsu (2015).

Contrary to Mavrommatis et al. (2014), Mavrommatis et al. (2015), and Yokota and Koketsu (2015), we here consider several transient deformation events (SSEs in Boso and offshore Honshu, volcanic unrests, see list in Table 2), and correct for those events in the time series modeling (see Section 3.2): we therefore

compute the inter-SSE velocities and associated locking. To evaluate the impact of removing the SSEs, we additionally compute the inter-seismic velocities and the associated locking without correcting for the SSEs in the trajectory model (Figures S17a and S18a in Supporting Information S1). As expected, the changes between both models are mainly located around the Boso SSEs area (Figures S17b and S18b in Supporting Information S1). However, the changes extend to the North due to the Tohoku SSE. The changes are tiny and involve an area that is larger than the strict extent of the SSEs because of the inversion smoothing and because the SSEs can be seen in a wide range of stations. On the PAC plate interface, the inter-SSE model is more locked than the inter-seismic model by ~ 0.02 under the Boso SSEs area (Figure S17b in Supporting Information S1). For the PHS plate, the locking is on average larger in the inter-SSE model by ~ 0.05 (Figure S18b in Supporting Information S1). These results can be explained by the fact that the SSEs contribute to the release of some of the accumulated slip.

More importantly, we find that not considering the Boso SSEs nor the Tohoku SSE during the computation of the trajectory model increases even further the slip acceleration on the PAC plate in the wider Kanto region (Figure S19 in Supporting Information S1).

Tanaka and Yabe (2017) also study the surface displacement and the seismicity in the Kanto area. They identify two long-term SSEs on the PHS plate with durations of 3–5 years: one before 2000 and the other after 2007. The main difference between their processing and ours is the modeling of the post-seismic transient and the SSEs. Tanaka and Yabe (2017) use an exponential model for the post-seismic transient as well as for the SSEs, while we use a logarithm model for the post-seismic transient (Equation 1) and a cosinus-like model for the SSEs (Equation 2). While we study the long-term acceleration over the whole 1997–2011 period, Tanaka and Yabe (2017) focus on smaller variations during this time period. Looking at our time series, the noise of the GPS data before 2000 prevent us to see the first SSE that Tanaka and Yabe (2017) identify. For the second one, after 2007, we do not see a clear signal in our time series residuals. Nevertheless, we notice the occurrence of the 2008 M_w 7.0 Ibaraki earthquake during the SSE and thus hypothesize that a more careful investigation of the 2008 M_w 7.0 Ibaraki earthquake post-seismic transient model would likely allow to better discriminate the post-seismic transient from the SSE observed by Tanaka and Yabe (2017). The acceleration we infer in the Kanto region includes the slip area inferred by Tanaka and Yabe (2017) for both SSEs. We showed in this section that if SSEs were not modeled, a stronger acceleration would result from our analysis. Thus our results are compatible with the observations of Tanaka and Yabe (2017), in the sense that our long-term acceleration could equally be interpreted as long-duration SSEs with a total accommodated slip which rate would accelerate at the 14-year scale. Moreover, the background seismicity used by Tanaka and Yabe (2017) to support their SSEs observations show an acceleration coherent with our seismic study (Section 6).

6. Seismicity Acceleration and Slip Acceleration

The confirmation of acceleration slip allows us to relate it to the concomitant acceleration of seismicity. To do so, and as with the GPS time series, aftershock sequences must be removed from the data, as they would otherwise dominate the activity. This is traditionally done by using declustering methods. This approach was followed by Marsan et al. (2017), who studied how the rate of background earthquakes changed along the Japan Trench from 1990 to 2011. They made use of two distinct declustering methods, so to only keep acceleration patterns that remain robust with regard to the specific assumptions underlying each of these methods. As a result, locations with incoherent acceleration values obtained with these two methods were discarded from the analysis. This becomes a problem for our analysis as large parts of the PAC slip interface are discarded, and cannot then be used to construct a seismic prior, unless applying specific smoothing constraints. We therefore re-analyze the seismicity, by (a) keeping all the 1997–2011 (up to March) earthquakes within 20 km of the PAC slip interface; (b) using the same regular grid as with our slip inversions; (c) selecting at each grid node (center of the triangle patches) the earthquakes within a radius of 100 km (hence an earthquake can be used at several neighboring nodes) and extending this range if necessary until finding 500 earthquakes; and (d) model all the obtained time series with an earthquake rate:

$$\lambda_j(t) = \mu_j(t) + \sum_{i|t_i < t, m_i \geq 7} K_{ij}(t + c_i - t_i)^{-p_i} \quad (15)$$

where λ_j is the modeled rate at node j , $\mu_j(t) = a_j t + b_j$ is the background rate (that includes an acceleration/deceleration parameter a), and where the sum is done on all magnitude 7.0 or greater earthquake i . In this model, each $M 7+$ mainshock can affect all the nodes, but the Omori's parameters p_i and c_i are kept the same for all nodes, for a given mainshock i . We optimize the parameters a_j , b_j , c_i , p_i , and K_{ij} given the data, constraining $\mu_j(t)$ to always be positive (which does not imply that a itself must be positive). We then compare the space-varying seismicity acceleration parameter a with our inverted slip rate changes. We measure the seismicity acceleration with:

$$\phi_j = \frac{\mu_j(t = 09 \text{ Mar } 2011)}{\mu_j(t = 01 \text{ Jan } 1997)} \quad (16)$$

Figure 7a shows the spatial variations of the seismicity acceleration and Figure S20 in Supporting Information S1 shows the temporal evolution of the seismicity at 10 patches.

We convert this seismicity acceleration into the a priori expected slip acceleration over the same period, defining a new prior model as shown in Figure 7c. This conversion is based on the assumption that the slip rate (dx_{slip}/dt) and the background seismicity rate (μ) are proportional (the proportionality coefficient is assumed constant in time, but is allowed to vary spatially). This factor would likely be controlled by physical parameters, including the size distribution and density of asperities, the resulting seismic coupling at the local scale, and so on. In our modeling, the modeled slip rate is $dx_{slip}/dt = v_{slip} + a_{slip}(t - t_R)$; we thus have for any initial t_1 and ending t_2 dates:

$$\phi = \frac{v_{slip} + a_{slip}(t_2 - t_R)}{v_{slip} + a_{slip}(t_1 - t_R)} \quad (17)$$

We here use $t_1 = 1997$ so that $t_1 = t_R$ (same reference time than for Equation 1), and $t_2 = 2011.1$. We thus get that the slip acceleration when comparing slip rate at those t_1 and t_2 is:

$$a_{slip} = (\phi - 1) \frac{v_{slip}}{t_2 - t_R} \quad (18)$$

with $v_{slip} = (1 - L) \times v_{PAC}$ where L is the locking coefficient and $v_{PAC} = 76$ mm/yr. As we only examine changes over time, this approach allows to discard the unknown proportionality coefficient between the slip and seismicity rates.

The slip acceleration prior obtained using our analysis of the seismicity is shown in Figure 7c, and show good correlation with the already inverted slip acceleration of Figure 6, with the notable exception of the downdip 36.5°–39°N latitude range, for which seismicity acceleration is very clear and significant, while our slip inversion finds an overall deceleration. Seismicity in the co-seismic zone of the 2011 Tohoku earthquake is not strong during the 1997–2011 (up to March) period, as can be expected given the high degree of inter-seismic locking there, and the seismicity acceleration is very mild compared to the inverted slip rate change.

Mavrommatis et al. (2015) also studied the acceleration in the seismicity but using repeating earthquake time series. Our seismic prior displays the same large-scale features, although the strong downdip acceleration we find is observed more updip in their analysis. Also, and contrary to them, we find a strong acceleration in the Kanto region and offshore Kanto. This particular feature is discussed in more detail in Section 7.

We show the inverted slip acceleration field using this seismic prior in Figure 7d. The locking used to compute the prior values in Figure 7b is the one obtained with a fully locked prior model; Figure S21 in Supporting Information S1 shows the results using the locking as given by a fully unlocked prior model. The accelerated slip obtained using the seismic prior shows similar features to the one shown in Figure 6. A noticeable change is the more focused acceleration in the Boso area, which now appears separated from the acceleration patch in the updip 36°–38°N area.

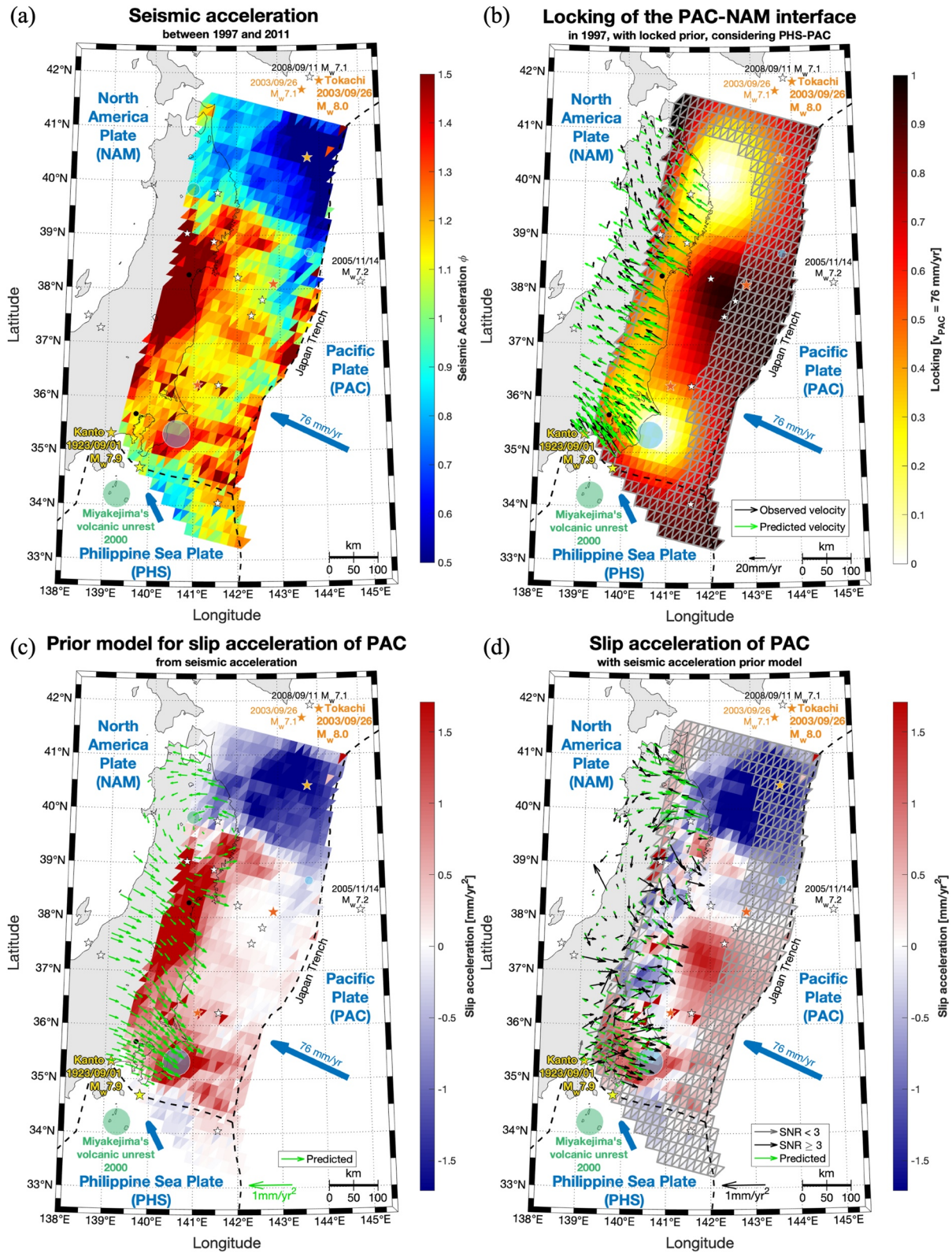


Figure 7.

7. Discussion and Conclusion

Our analysis completes previous similar studies (Heki & Mitsui, 2013; Loveless & Meade, 2010; Mavrommatis et al., 2014; Yokota & Koketsu, 2015) in several ways: (a) by testing different methods for computing the daily GPS solution; (b) by accounting for SSEs as well as volcanic unrests: these transients were removed from the GPS time series (Section 3.2), even though this change in the modeling is not the reason for the acceleration found (cf. Section 5.3.2); (c) by including the PHS slip interface underneath Kanto and along the Sagami Trough (as shown in Figure 4b), even if this addition does not significantly modify the results obtained with the PAC plate alone (see Section 5.2.3 and Figure S14 in Supporting Information S1); (d) by adding prior information based on background seismicity changes (Section 6). From this, we confirm and strengthen the robustness of previous observations, mainly relating to a significant acceleration of the slip for the PAC subduction, in the range of 1.5–2.5 mm/yr² centered at 37°–38°N, and corresponding to the downdip extension of the area that slipped by more than 30 m during the 2011 M_w 9.0 Tohoku earthquake. Such a slip acceleration corresponds to a decrease in coupling of the order of -0.2 – -0.3 over the 1997–2011 period (Figure 5). This area is well delineated by a marked reversal in sign of the acceleration to the north: all tested models (Figures 6 and 7) find a robust slip deceleration of ~ 3 mm/yr² north of 39°N, which origin could be related to the 1994 Sanriku earthquake and subsequent afterslip (Heki et al., 1997) and/or to the 2003 Tokachi earthquake (Heki & Mitsui, 2013).

It must be argued here that our inversions of the slip rate acceleration assumed a fully elastic medium. Visco-elasticity from the lower crust downwards could affect this inversion, especially as the time scale of our study (14 years) is comparable to typical Maxwell characteristic times in subduction modeling (Wang et al., 2012). A full investigation of visco-elastic models is however beyond the scope of the present study.

It has been argued by Hasegawa and Yoshida (2015) that the downdip acceleration (between 37° and 38°N) must have contributed to further stressing of the main asperity that eventually failed in 2011. Whether this acceleration is a common phenomenon in this region or cannot be answered with certainty. Hildebeck (2012) discusses the near complete release of the differential stress at the time of the 2011 shock. The released seismic moment only amounts to a 0.23–0.77 proportion of the moment that accumulated in the 1,142 years since the last equivalent megathrust earthquake in this region, the 869 CE Jogan earthquake that triggered a tsunami with comparable characteristics to those of the 2011 Tohoku event (Minoura et al., 2001, 2013; Sugawara et al., 2012). Indeed, even accounting for large post-seismic relaxation lasting several decades, as seen after the 1960 Chile earthquake (Melnick et al., 2018; Wang et al., 2007), as well as incomplete plate coupling, a M_w 9 earthquake would need to occur every 300–700 years to match the average modeled rate of moment accumulation (Ozawa et al., 2012). The stressing rate (hence the slip rate on the interface) is thus likely to vary during the extended inter-seismic period. The short-term (i.e., over 14 years) average coupling could then be an overestimation of the longer time-averaged coupling. The fact that we infer a 14-year long decrease of coupling (even after removing co-seismic and post-seismic effects of the intermediate size earthquakes that have occurred in the region during this time period) is coherent with the fact that there must exist significant variations of coupling during the earthquake cycle in this region.

A novel feature of our analysis is the broad slip acceleration in the 35° to 36°N area, although weaker (by a factor 2) than for the 37°–38°N region. This was not identified by previous studies, although this is a robust feature of our inversions (Figures 6 and 7). Even though some trade-off exists between changes in slip rate along the PAC-NAM and the PHS-NAM interfaces, our analysis suggests that the slip acceleration along the former dominates (Figure 6 and Figure S14 in Supporting Information S1). Slip acceleration along the PHS-NAM interface is however independently suggested by the acceleration of seismicity documented in Reverso et al. (2016) offshore Boso, as well as the shortening of the Boso SSE recurrence interval that took place between 1996 and 2014, and which can be seen as the signature of an increasing loading in this area (Fukuda, 2018; Hirose et al., 2012; Ozawa, 2014).

Figure 7. Seismicity acceleration of the Pacific (PAC) plate between 1997 and 2011 as slip acceleration prior. (a) Seismicity acceleration of the Pacific (PAC) plate between 1997 and 2011; the color scale gives the acceleration value ϕ of the seismicity rate: blue ($\phi < 1$) represents deceleration and red ($\phi > 1$) acceleration. (b) Locking of the Pacific-North America (PAC-NAM) interface in 1997, with a fully locked prior model; same legend as Figure 4. (c) Prior slip acceleration model of the PAC plate based on the seismicity acceleration (a) and the locking (b) with Equation 18; same legend as Figure 6. (d) Slip acceleration of the PAC plate with (c) as prior slip acceleration model; same legend as Figure 6. Other elements are described in Figure 1.

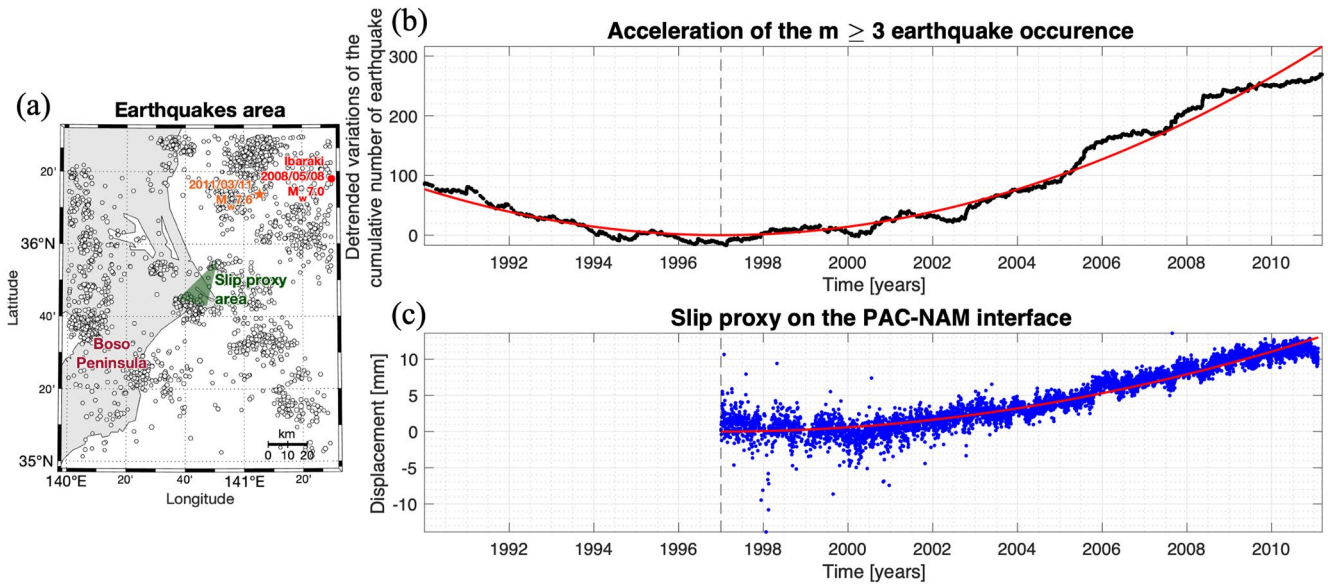


Figure 8. Acceleration of $m \geq 3$ earthquakes within 10 km of the Pacific-North America (PAC-NAM) interface (b) in the 35° – 36.5° N, 140° – 141.5° E box (a), for the 1990–March 2011 period compared with a slip proxy on the PAC-NAM interface at the green patch in the center of the box (a). (a) The white circles represent $m \geq 3$ earthquakes within 10 km of the PAC-NAM interface, the red circle represents the 2008 M_w 7.0 Ibaraki earthquake, the green triangle represents the slip proxy area (corresponding to the black H patch in Figure S20 in Supporting Information S1), and other elements are described in Figure 1. (b) The black dots represent the detrended variation of the cumulative number of $m \geq 3$ earthquakes. The quadratic fit is shown in red, and gives an acceleration in seismicity rate of +86% for 1990–2011 and +44% for 1997–2011 (the vertical dashed line shows the January 1, 1997 date). (c) The blue dots represent the slip proxy from 1997 to 2011. The quadratic fit is shown in red, and gives an acceleration of 0.065 mm/yr^2 .

Compared to the rest of our studied area, this zone is characterized by small earthquakes, with the noticeable exception of the 2008 M_w 7.0 Ibaraki earthquake. Because of this absence of strong shocks that would create transient increases in earthquake rate, the seismicity dynamics is relatively smooth, and is not dominated by strong aftershock sequences, as is on the contrary observed more to the north (Ozawa et al., 2012). A direct analysis of the seismicity ($m \geq 3$) rate can thus be conducted at first order without having to correct for aftershock sequences. Figure 8b confirms the existence of a significant acceleration of the earthquake rate in the region from 35° to 36.5° N and 140° to 141.5° E, that cannot be attributed to the 2008 Ibaraki mainshock and its aftershock sequence, as it occurs relatively late in the considered 1990–2011 interval. Figure 8c shows a proxy for the slip on the PAC-NAM interface in the area that can be directly compared with the seismicity acceleration in this region. This slip proxy S is computed as a simple stack of the surface position time series (to which the linear trajectory model has been removed) weighted by the values of the elastic Green function matrix for a patch j located at the center of the area:

$$S_j(t) = \frac{\sum_i G_{ij} d_i(t)}{\sum_i G_{ij}} \quad (19)$$

where d_i is the displacement at each station i and G_{ij} are the values of the Green function that link the patch j to each station i . For an easier comparison of the observed variations, we have detrended both the cumulative seismicity and stacked displacement (slip proxy) time series with their rate value in 1997 (the beginning of our position time series). The most striking resemblance between seismicity and displacement time series is the long-term acceleration, that is clearly visible on both time series. Also, although the stacked displacements are more noisy, we observe burst-like variations around the quadratic fit in both the seismicity and displacement time series. Some of these burst-like variations even appear temporally correlated between deformation and seismicity.

This area is known for its SSEs offshore Boso, which are associated with seismicity swarms (Hirose et al., 2012) both on the PHS-NAM. The burst-like behavior in the seismicity rate could be the signature of smaller SSEs (or temporal changes in locking) that have escaped detection through GPS measurements (Gardonio et al., 2018; Reverso et al., 2016), and that may play a role in the nucleation of large earthquakes,

as suggested for the PAC-NAM interface by Nishikawa and Ide (2018) in the case of the 2008 M_w 7.0 Ibaraki earthquake. Intermittent slow slip therefore seems significant in this region, and accelerated seismicity could thus imply an acceleration of the controlling aseismic forcing rate. Given the mechanical coupling (i.e., contact) between the PAC and PHS plates offshore Boso, this interpretation is coherent with (a) the strong acceleration in background rate observed by Marsan et al. (2017) over the 1990–2011 period, (b) the remarkable acceleration in seismicity rate in the Boso area for the same period (Reverso et al., 2016), as well as (c) the shortening of Boso inter-SSE periods of times (Ozawa, 2014). All these observations point to an unlocking of the PAC-NAM interface there, estimated to be about 0.2–0.3 as shown in Figure 5. We find that the slip rate decelerates along the PHS-NAM interface (Figure S14b in Supporting Information S1), in contradiction with the seismicity acceleration and SSE interval shortening. The smoothing performed by the inversion procedure implies a nearly uniform slip rate change over the modeled PHS plate, although the geometrical complexity of this plate (especially compared to PAC) could be expected to result in a more heterogeneous slip rate change; also, the inversion trade-off between the two PAC and PHS plates could hide more restricted areas of acceleration that would be compatible with the above observations of Ozawa (2014) and Reverso et al. (2016).

This inferred accelerated slip in the Kanto area is noticeably far from the 2011 rupture and remains therefore to be explained. It adds up to previous observations in other plate convergence contexts (Materna et al., 2019; Meltzner et al., 2015; Prawirodirdjo et al., 2010) that the slip rate, and thus the plate locking, could evolve significantly over years to decades outside the widely observed post-seismic slip following any mainshock.

Data Availability Statement

Raw time series data are accessible on the Observatoire des Sciences de l'Univers de Grenoble website associated to the DOI: <https://doi.org/10.17178/GNSS.products.Japan>.

Acknowledgments

The authors would like to thank Michel Bouchon, Mohamed Chlieh, Piero Poli, and Roland Burgmann for very valuable discussions and suggestions. This study has been supported by the Agence Nationale de la Recherche (ANR-17-CE31-0002-01) AtypicSSE project and by Université Savoie Mont-Blanc. The authors are very grateful to the Geospatial Information Authority of Japan (GSI) for making the GEONET GNSS data available. Most of the computations presented in this study were performed using the GRICAD infrastructure (https://gricad.univ-grenoble-alpes.fr/index_en.html), which is partly supported by the Equip@Meso project (reference ANR-10-EQPX-29-01) of the program Investissements d'Avenir supervised by the Agence Nationale pour la Recherche, and the CIMENT infrastructure (<https://ciment.ujf-grenoble.fr>), which is supported by the Rhône-Alpes region (Grant CPER07_13 CIRA) and France-Grille (<http://www.france-grilles.fr/home/>).

References

- Altamimi, Z., Collillieux, X., Legrand, J., Garayt, B., & Boucher, C. (2007). ITRF2005: A new release of the International Terrestrial Reference Frame based on time series of station positions and Earth Orientation Parameters. *Journal of Geophysical Research*, *112*, B09401. <https://doi.org/10.1029/2007JB004949>
- Altamimi, Z., Métivier, L., Rebischung, P., Rouby, H., & Collillieux, X. (2017). ITRF2014 plate motion model. *Geophysical Journal International*, *209*(3), 1906–1912. <https://doi.org/10.1093/gji/ggx136>
- Bevis, M., & Brown, A. (2014). Trajectory models and reference frames for crustal motion geodesy. *Journal of Geodesy*, *88*(3), 283–311. <https://doi.org/10.1007/s00190-013-0685-5>
- Boehm, J., Werl, B., & Schuh, H. (2006). Troposphere mapping functions for GPS and very long baseline interferometry from European Centre for Medium-Range Weather Forecasts operational analysis data. *Journal of Geophysical Research: Solid Earth*, *111*(B2). <https://doi.org/10.1029/2005JB003629>
- Cattania, C., Rivalta, E., Hainzl, S., Passarelli, L., & Aoki, Y. (2017). A nonplanar slow rupture episode during the 2000 Miyakejima dike intrusion. *Journal of Geophysical Research: Solid Earth*, *122*(3), 2054–2068. <https://doi.org/10.1002/2016JB013722>
- Fukuda, J. (2018). Variability of the space-time evolution of slow slip events off the Boso Peninsula, central Japan, from 1996 to 2014. *Journal of Geophysical Research: Solid Earth*, *123*, 732–760. <https://doi.org/10.1002/2017JB014709>
- Gardonio, B., Marsan, D., Bouchon, M., Socquet, A., Jara, J., Sun, Q., et al. (2018). Revisiting slow slip events occurrence in Boso Peninsula, Japan, combining GPS data and repeating earthquakes analysis. *Journal of Geophysical Research: Solid Earth*, *123*, 1502–1515. <https://doi.org/10.1002/2017JB014469>
- Hardebeck, J. L. (2012). Coseismic and postseismic stress rotations due to great subduction zone earthquakes. *Geophysical Research Letters*, *39*, L21313. <https://doi.org/10.1029/2012GL053438>
- Hasegawa, A., & Yoshida, K. (2015). Preceding seismic activity and slow slip events in the source area of the 2011 Mw 9.0 Tohoku-Oki earthquake: A review. *Geoscience Letters*, *2*(6). <https://doi.org/10.1186/s40562-015-0025-0>
- Hayes, G. P., Moore, G. L., Portner, D. E., Hearne, M., Flamme, H., Furtney, M., & Smoczyk, G. M. (2018). Slab2, a comprehensive subduction zone geometry model. *Science*, *362*(6410), 58–61. <https://doi.org/10.1126/science.aat4723>
- Heki, K., & Mitsui, Y. (2013). Accelerated Pacific plate subduction following interplate thrust earthquakes at the Japan trench. *Earth and Planetary Science Letters*, *363*, 44–49. <https://doi.org/10.1016/j.epsl.2012.12.031>
- Heki, K., Miyazaki, S., & Tsuji, H. (1997). Silent fault slip following an interplate thrust earthquake at the Japan trench. *Nature*, *386*(6625), 595–598. <https://doi.org/10.1038/386595a0>
- Herring, T. A., Floyd, M. A., King, R. W., & McClusky, S. C. (2015). GLOBK reference manual: Global Kalman filter VLBI and GPS analysis program: Release 10.6 [Computer software manual].
- Herring, T. A., King, R. W., Floyd, M. A., & McClusky, S. C. (2018a). GAMIT reference manual: GPS analysis at MIT: Release 10.7. [Computer software manual].
- Herring, T. A., King, R. W., Floyd, M. A., & McClusky, S. C. (2018b). Introduction to GAMIT/GLOBK: Release 10.7. [Computer software manual].

- Herring, T. A., Melbourne, T. I., Murray, M. H., Floyd, M. A., Szeliga, W. M., King, R. W., et al. (2016). Plate boundary observatory and related networks: GPS data analysis methods and geodetic products. *Reviews of Geophysics*, 54, 759–808. <https://doi.org/10.1002/2016RG000529>
- Hirose, H., Hirahara, K., Kimata, F., Fujii, N., & Miyazaki, S. (1999). A slow thrust slip event following the two 1996 Hyuganada earthquakes beneath the Bungo Channel, southwest Japan. *Geophysical Research Letters*, 26(21), 3237–3240. <https://doi.org/10.1029/1999GL010999>
- Hirose, H., Kimura, H., Enescu, B., & Aoi, S. (2012). Recurrent slow slip event likely hastened by the 2011 Tohoku earthquake. *Proceedings of the National Academy of Sciences of the United States of America*, 109(38), 15157–15161. <https://doi.org/10.1073/pnas.1202709109>
- Hooper, A., Pietrzak, J., Simons, W., Cui, H., Riva, R., Naeije, M., et al. (2013). Importance of horizontal seafloor motion on tsunami height for the 2011 Mw=9.0 Tohoku-Oki earthquake. *Earth and Planetary Science Letters*, 361, 469–479. <https://doi.org/10.1016/j.epsl.2012.11.013>
- Ishida, M. (1992). Geometry and relative motion of the Philippine Sea plate and Pacific plate beneath the Kanto-Tokai district, Japan. *Journal of Geophysical Research*, 97(B1), 489–513. <https://doi.org/10.1029/91JB02567>
- Ito, A., Fujie, G., Tsuru, T., Kodaira, S., Nakanishi, A., & Kaneda, Y. (2004). Fault plane geometry in the source region of the 1994 Sanriku-oki earthquake. *Earth and Planetary Science Letters*, 223(1–2), 163–175. <https://doi.org/10.1016/j.epsl.2004.04.007>
- Ito, T., & Yoshioka, S. (2002). A dike intrusion model in and around Miyakejima, Niijima and Kozushima in 2000. *Tectonophysics*, 359, 171–187. [https://doi.org/10.1016/S0040-1951\(02\)00510-3](https://doi.org/10.1016/S0040-1951(02)00510-3)
- Ito, Y., Hino, R., Kido, M., Osada, Y., Inazu, D., Ohta, Y., et al. (2013). Episodic slow slip events in the Japan subduction zone before the 2011 Tohoku-Oki earthquake. *Tectonophysics*, 600, 14–26. <https://doi.org/10.1016/j.tecto.2012.08.022>
- Kobayashi, A. (2014). A long-term slow slip event from 1996 to 1997 in the Kii Channel, Japan. *Earth, Planets and Space*, 66(9). <https://doi.org/10.1186/1880-5981-66-9>
- Kobayashi, A., & Tsuyuki, T. (2019). Long-term slow slip event detected beneath the Shima Peninsula, central Japan, from GNSS data. *Earth, Planets and Space*, 71(60). <https://doi.org/10.1186/s40623-019-1037-3>
- Komori, J., Shishikura, M., Ando, R., Yokoyama, Y., & Miyairi, Y. (2017). History of the great Kanto earthquakes inferred from the ages of Holocene marine terraces revealed by a comprehensive drilling survey. *Earth and Planetary Science Letters*, 471, 74–84. <https://doi.org/10.1016/j.epsl.2017.04.044>
- Kositsky, A. P., & Avouac, J.-P. (2010). Inverting geodetic time series with a principal component analysis-based inversion method. *Journal of Geophysical Research*, 115, B03401. <https://doi.org/10.1029/2009JB006535>
- Lay, T. (2018). A review of the rupture characteristics of the 2011 Tohoku-Oki Mw 9.1 earthquake. *Tectonophysics*, 733, 4–36. <https://doi.org/10.1016/j.tecto.2017.09.022>
- Li, S., Freymueller, J., & McCaffrey, R. (2016). Slow slip events and time-dependent variations in locking beneath Lower Cook Inlet of the Alaska-Aleutian subduction zone. *Journal of Geophysical Research: Solid Earth*, 121, 1060–1079. <https://doi.org/10.1002/2015JB012491>
- Loveless, J. P., & Meade, B. J. (2010). Geodetic imaging of plate motions, slip rates, and partitioning of deformation in Japan. *Journal of Geophysical Research*, 115, B02410. <https://doi.org/10.1029/2008JB006248>
- Loveless, J. P., & Meade, B. J. (2016). Two decades of spatiotemporal variations in subduction zone coupling offshore Japan. *Earth and Planetary Science Letters*, 436, 19–30. <https://doi.org/10.1016/j.epsl.2015.12.033>
- Mallick, R., Meltzner, A. J., Tsang, L. L. H., Lindsey, E. O., Feng, L., & Hill, E. M. (2021). Long-lived shallow slow-slip events on the Sunda megathrust. *Nature Geoscience*, 14(5), 327–333. <https://doi.org/10.1038/s41561-021-00727-y>
- Marsan, D., Bouchon, M., Gardonio, B., Perfettini, H., Socquet, A., & Enescu, B. (2017). Change in seismicity along the Japan trench, 1990–2011, and its relationship with seismic coupling. *Journal of Geophysical Research: Solid Earth*, 122, 4645–4659. <https://doi.org/10.1002/2016JB013715>
- Materna, K., Bartlow, N., Wech, A., Williams, C., & Bürgmann, R. (2019). Dynamically triggered changes of plate interface coupling in Southern Cascadia. *Geophysical Research Letters*, 46(12), 12890–12899. <https://doi.org/10.1029/2019GL084395>
- Mavrommatis, A. P., Segall, P., & Johnson, K. M. (2014). A decadal-scale deformation transient prior to the 2011 Mw 9.0 Tohoku-Oki earthquake. *Geophysical Research Letters*, 41, 4486–4494. <https://doi.org/10.1002/2014GL060139>
- Mavrommatis, A. P., Segall, P., Uchida, N., & Johnson, K. M. (2015). Long-term acceleration of aseismic slip preceding the Mw 9 Tohoku-Oki earthquake: Constraints from repeating earthquakes. *Geophysical Research Letters*, 42, 9717–9725. <https://doi.org/10.1002/2015GL066069>
- Melnick, D., Li, S., Moreno, M., Cisternas, M., Jara-Muñoz, J., Wesson, R., et al. (2018). Back to full interseismic plate locking decades after the giant 1960 Chile earthquake. *Nature Communications*, 9, 3527. <https://doi.org/10.1038/s41467-018-05989-6>
- Melnick, D., Moreno, M., Quinteros, J., Baez, J. C., Deng, Z., Li, S., & Oncken, O. (2017). The super-interseismic phase of the megathrust earthquake cycle in Chile. *Geophysical Research Letters*, 44, 784–791. <https://doi.org/10.1002/2016GL071845>
- Meltzner, A. J., Sieh, K., Chiang, H.-W., Wu, C.-C., Tsang, L. L., Shen, C.-C., et al. (2015). Time-varying interseismic strain rates and similar seismic ruptures on the Nias-Simeulue patch of the Sunda megathrust. *Quaternary Science Reviews*, 122, 258–281. <https://doi.org/10.1016/j.quascirev.2015.06.003>
- Minoura, K., Hirano, S.-I., & Yamada, T. (2013). Identification and possible recurrence of an oversized tsunami on the Pacific coast of northern Japan. *Natural Hazards*, 68, 631–643. <https://doi.org/10.1007/s11069-013-0640-z>
- Minoura, K., Imamura, F., Sugawara, D., Kono, Y., & Iwashita, T. (2001). The 869 Jogan tsunami deposit and recurrence interval of large-scale tsunami on the Pacific coast of northeast Japan. *Journal of Natural Disaster Science*, 23(2), 83–88.
- Miura, S., Ueki, S., Sato, T., Tachibana, K., & Hamaguchi, H. (2000). Crustal deformation associated with the 1998 seismo-volcanic crisis of Iwate Volcano, Northeastern Japan, as observed by a dense GPS network. *Earth, Planets and Space*, 52, 1003–1008. <https://doi.org/10.1186/bf03352321>
- Miyazaki, S., McGuire, J. J., & Segall, P. (2003). A transient subduction zone slip episode in southwest Japan observed by the nationwide GPS array. *Journal of Geophysical Research*, 108(B2), 2087. <https://doi.org/10.1029/2001JB000456>
- Nakada, S., Nagai, M., Kaneko, T., Nozawa, A., & Suzuki-Kamata, K. (2005). Chronology and products of the 2000 eruption of Miyakejima Volcano, Japan. *Bulletin of Volcanology*, 67, 205–218. <https://doi.org/10.1007/s00445-004-0404-4>
- Nakagawa, H., Toyofuku, T., Kotani, K., Miyahara, B., Iwashita, C., Kawamoto, S., & Suguwara, Y. (2009). Development and validation of GEONET new analysis strategy (Version 4) [in Japanese]. *Journal of the Geographical Survey Institute*, 118, 1–8.
- Nishikawa, T., & Ide, S. (2018). Recurring slow slip events and earthquake nucleation in the source region of the m 7 Ibaraki-Oki earthquakes revealed by earthquake swarm and foreshock activity. *Journal of Geophysical Research: Solid Earth*, 123, 7950–7968. <https://doi.org/10.1029/2018JB015642>
- Nishimura, T., Sagiya, T., & Stein, R. S. (2007). Crustal block kinematics and seismic potential of the northernmost Philippine Sea plate and Izu microplate, central Japan, inferred from GPS and leveling data. *Journal of Geophysical Research*, 112, B05414. <https://doi.org/10.1029/2005JB004102>

- Ochi, T., & Kato, T. (2013). Depth extent of the long-term slow slip event in the Tokai district, central Japan: A new insight. *Journal of Geophysical Research: Solid Earth*, *118*, 4847–4860. <https://doi.org/10.1002/jgrb.50355>
- Okada, Y. (1985). Surface deformation due to shear and tensile faults in a half-space. *Bulletin of the Seismological Society of America*, *75*(4), 1135–1154. [https://doi.org/10.1016/0148-9062\(86\)90674-1](https://doi.org/10.1016/0148-9062(86)90674-1)
- Ozawa, S. (2014). Shortening of recurrence interval of Boso slow slip events in Japan. *Geophysical Research Letters*, *41*, 2762–2768. <https://doi.org/10.1002/2014GL060072>
- Ozawa, S., Murakami, M., & Tada, T. (2001). Time-dependent inversion study of the slow thrust event in the Nankai trough subduction zone, southwestern Japan. *Journal of Geophysical Research: Solid Earth*, *106*(B1), 787–802. <https://doi.org/10.1029/2000JB900317>
- Ozawa, S., Nishimura, T., Munekane, H., Suito, H., Kobayashi, T., Tobita, M., & Imakiire, T. (2012). Preceding, coseismic, and postseismic slips of the 2011 Tohoku earthquake, Japan. *Journal of Geophysical Research*, *117*, B07404. <https://doi.org/10.1029/2011JB009120>
- Ozawa, S., Suito, H., Imakiire, T., & Murakami, M. (2007). Spatiotemporal evolution of aseismic interplate slip between 1996 and 1998 and between 2002 and 2004, in Bungo channel, southwest Japan. *Journal of Geophysical Research*, *112*, B05409. <https://doi.org/10.1029/2006JB004643>
- Ozawa, S., Suito, H., & Tobita, M. (2007). Occurrence of quasi-periodic slow-slip off the east coast of the Boso peninsula, Central Japan. *Earth Planets and Space*, *59*, 1241–1245. <https://doi.org/10.1186/BF03352072>
- Ozawa, S., Yari, H., Imakiire, T., & Tobita, M. (2013). Spatial and temporal evolution of the long-term slow slip in the Bungo Channel, Japan. *Earth, Planets and Space*, *65*, 67–73. <https://doi.org/10.5047/eps.2012.06.009>
- Philibosian, B., & Meltzner, A. J. (2020). Segmentation and supercycles: A catalog of earthquake rupture patterns from the Sumatran Sunda Megathrust and other well-studied faults worldwide. *Quaternary Science Reviews*, *241*, 106390. <https://doi.org/10.1016/j.quascirev.2020.106390>
- Prawirodirjo, L., McCaffrey, R., Chadwell, C. D., Bock, Y., & Subarya, C. (2010). Geodetic observations of an earthquake cycle at the Sumatra subduction zone: Role of interseismic strain segmentation. *Journal of Geophysical Research*, *115*, B03414. <https://doi.org/10.1029/2008JB006139>
- Radiguet, M., Cotton, F., Vergnolle, M., Campillo, M., Valette, B., Kostoglodov, V., & Cotte, N. (2011). Spatial and temporal evolution of a long term slow slip event: The 2006 Guerrero Slow Slip Event. *Geophysical Journal International*, *184*, 816–828. <https://doi.org/10.1111/j.1365-246X.2010.04866.x>
- Reverso, T., Marsan, D., Helmstetter, A., & Enescu, B. (2016). Background seismicity in Boso Peninsula, Japan: Long-term acceleration, and relationship with slow slip events. *Geophysical Research Letters*, *43*, 5671–5679. <https://doi.org/10.1002/2016GL068524>
- Roussel, B., Fu, Y., Bartlow, N., & Bürgmann, R. (2019). Weeks-long and years-long slow slip and tectonic tremor episodes on the south central Alaska megathrust. *Journal of Geophysical Research: Solid Earth*, *124*(13), 13392–13403. <https://doi.org/10.1029/2019JB018724>
- Ruiz, S., Moreno, M., Melnick, D., del Campo, F., Poli, P., Baez, J. C., et al. (2017). Reawakening of large earthquakes in south central Chile: The 2016 Mw 7.6 Chiloé event. *Geophysical Research Letters*, *44*, 6633–6640. <https://doi.org/10.1002/2017GL074133>
- Savage, J. C., & Thatcher, W. (1992). Interseismic deformation at the Nankai Trough, Japan, subduction zone. *Journal of Geophysical Research*, *97*(B7), 11,117–11,135. <https://doi.org/10.1029/92JB00810>
- Shishikura, M. (2014). History of the paleo-earthquakes along the Sagami Trough, central Japan: Review of coastal paleo-seismological studies in the Kanto region. *Episodes*, *37*(4), 246–257. <https://doi.org/10.18814/epiiugs/2014/v37i4/004>
- Sugawara, D., Goto, K., Imamura, F., Matsumoto, H., & Minoura, K. (2012). Assessing the magnitude of the 869 Jogan tsunami using sedimentary deposits: Prediction and consequence of the 2011 Tohoku-Oki tsunami. *Sedimentary Geology*, *282*, 14–26. <https://doi.org/10.1016/j.sedgeo.2012.08.001>
- Suito, H., Nishimura, T., Tobita, M., Imakiire, T., Ozawa, S., & Sieh, K. (2011). A 15 year slow-slip event on the Sunda megathrust offshore Sumatra. *Geophysical Research Letters*, *42*(16), 6630–6638. <https://doi.org/10.1002/2015GL064928>
- Tanaka, Y., & Yabe, S. (2017). Two long-term slow slip events around Tokyo Bay found by GNSS observation during 1996–2011. *Earth, Planets and Space*, *69*(43). <https://doi.org/10.1186/s40623-017-0628-0>
- Tarantola, A., & Valette, B. (1982). Generalized nonlinear inverse problems solved using the least squares criterion. *Reviews of Geophysics and Space Physics*, *20*(2), 219–232. <https://doi.org/10.1029/RG020i002p00219>
- Tran, D. T. (2009). *Analyse rapide et robuste des solutions GPS pour la tectonique [in French] (Doctoral dissertation)*. Université de Nice-Sophia Antipolis.
- Tsang, L. L. H., Meltzner, A. J., Philibosian, B., Hill, E. M., Freymueller, J. T., & Sieh, K. (2015). A 15 year slow-slip event on the Sunda megathrust offshore Sumatra. *Geophysical Research Letters*, *42*(16), 6630–6638. <https://doi.org/10.1002/2015GL064928>
- Tsuji, H., Hatanaka, Y., Hiyama, Y., Yamaguchi, K., Furuya, T., Kawamoto, S., & Fukuzaki, Y. (2017). Twenty-year successful operation of GEONET. *Bulletin of the Geospatial Information Authority of Japan*, *65*, 19–44.
- Uehira, K., Baba, T., Mori, H., Katayama, H., & Hamada, N. (2005). Earthquake swarms preceding the 2000 eruption of Miyakejima volcano, Japan. *Bulletin of Volcanology*, *67*, 219–230. <https://doi.org/10.1007/s00445-004-0405-3>
- Wang, K., Hu, Y., Bevis, M., Kendrick, E., Smalley, R., Vargas, R. B., & Lauria, E. (2007). Crustal motion in the zone of the 1960 Chile earthquake: Detangling earthquake-cycle deformation and forearc-sliver translation. *Geochemistry, Geophysics, Geosystems*, *8*(10). <https://doi.org/10.1029/2007GC001721>
- Wang, K., Hu, Y., & He, J. (2012). Deformation cycles of subduction earthquakes in a viscoelastic Earth. *Nature*, *484*(7394), 327–332. <https://doi.org/10.1038/nature11032>
- Yagi, Y., & Kikuchi, M. (2003). Partitioning between seismogenic and aseismic slip as highlighted from slow slip events in Hyuga-nada, Japan. *Geophysical Research Letters*, *30*(2), 1087. <https://doi.org/10.1029/2002GL015664>
- Yamanaka, Y., & Kikuchi, M. (2003). Source process of the recurrent Tokachi-oki earthquake on September 26, 2003, inferred from teleseismic body waves. *Earth, Planets and Space*, *55*, e21–e24. <https://doi.org/10.1186/BF03352479>
- Yokota, Y., & Koketsu, K. (2015). A very long-term transient event preceding the 2011 Tohoku earthquake. *Nature Communications*, *6*(5934). <https://doi.org/10.1038/ncomms6934>
- Yoshioka, S., Matsuoka, Y., & Ide, S. (2015). Spatiotemporal slip distributions of three long-term slow slip events beneath the Bungo Channel, southwest Japan, inferred from inversion analyses of GPS data. *Geophysical Journal International*, *201*, 1437–1455. <https://doi.org/10.1093/gji/ggv022>